Modelling Simul. Mater. Sci. Eng. 1 (1992) 225–263. Printed in the UK

REVIEW ARTICLE

Computational modelling of single crystals

A M Cuitiño and M Ortiz†
Division of Engineering, Brown University, Providence, RI 02912, USA

Received 26 June 1992, accepted for publication 8 October 1992

Abstract. The physical basis of computationally tractable models of crystalline plasticity is reviewed. A statistical mechanical model of dislocation motion through forest dislocations is formulated. Following Franciosi and co-workers, the strength of the short-range obstacles introduced by the forest dislocations is allowed to depend on the mode of interaction. The kinetic equations governing dislocation motion are solved in closed form for monotonic loading, with transients in the density of forest dislocations accounted for. This solution, coupled with suitable equations of evolution for the dislocation densities, provides a complete description of the hardening of crystals under monotonic loading. Detailed comparisons with experiment demonstrate the predictive capabilities of the theory. An adaptive finite element formulation for the analysis of ductile single crystals is also developed. Calculations of the near-tip fields in Cu single crystals illustrate the versatility of the method.

1. Introduction

Ductile single crystals are of considerable interest in single-phase form, e.g. as structural materials in propeller and turbine blades, or as basic building blocks of numerous material systems, such as polycrystalline metals and igneous rocks. Many deformation processes of interest take place at the single-crystal level. Notable examples include the development of deformation textures in polycrystalline metals, shear band formation within grains, crack nucleation and growth at grain boundaries, transgranular cracking, and others. Recent advances in computer hardware and software have made ever more detailed simulations of ductile single crystals and polycrystals possible. Impetus for this type of simulation is provided by a desire to root models of the behavior of solids on a sound micromechanical basis. There is, therefore, a need for computationally tractable models which emanate directly from a clear micromechanical picture, as well as for robust and versatile computational techniques for incorporating the models into numerical simulations.

Our first aim here is to review dislocation theories which, in combination, point to a plausible form of the hardening relations for single crystals. The theories considered concern: (i) the motion of a dislocation line through forest dislocations; (ii) the short-range interactions between pairs of dislocations and the strength of the resulting intersections viewed as point obstacles, and (iii) the kinetics of dislocation multiplication. It bears emphasis that, in the simple physical picture contemplated here, hardening is assumed to be primarily the effect of forest dislocations. Simple though it may be, a satisfactory aspect of this theory is that it is amenable to a rather rigorous analytical treatment within the framework of non-equilibrium statistical mechanics.

† e-mail: ortiz@en604r.engin.brown.edu

0965-0393/92/030225+39$07.50

Indeed, we show that, for monotonic loading, the kinetic equation governing the percolation-like motion of a dislocation line through a random array of point obstacles can be solved in closed form. Our solution includes the case in which the density of point obstacles is a function of time. Following Franciosi and co-workers (Franciosi *et al* 1980, Franciosi and Zaoui 1982, Franciosi 1983, 1985a,b, 1988), the strength of the short-range obstacles introduced by forest dislocations is taken to be a function of the mode of interaction, e.g. of whether the intersecting dislocations react to form junctions. Our analytical solution, in conjunction with Franciosi's relations, completely determines the hardening relations of the crystal in terms of the density of dislocations in all slip systems. To obtain a closed set of constitutive relations, we draw on the work of Gillis and Gilman (1965) and Essmann and Rapp (1973) to formulate the requisite equations of evolution for the dislocation densities as a function of slip activity.

Interestingly, the dislocation-based model reconciles some apparent differences between the recent work of Bassani and Wu (Wu *et al* 1989, Bassani and Wu 1989, Bassani 1990), who have proposed a model in which the hardening matrix is diagonally dominant, and the more conventional approach of Pierce and co-workers (Pierce *et al* 1983), who model latent-hardening effects by means of a hardening matrix in which the off-diagonal terms are dominant. These two models arise from seemingly diverging interpretations of the experimental record. The dislocation model developed here suggests that these views are, in fact, complementary. Thus, for each slip system, two characteristic resolved shear stresses can be identified: the elastic limit, or yield stress; and a characteristic stress roughly coincident with the value of flow stress obtained by back-extrapolation of the stress–strain curve, a procedure which is commonly adopted for the interpretation of latent hardening experiments (Kocks 1970, Ramaswami *et al* 1965, Kocks and Brown 1966, Franciosi *et al* 1980, Bassani 1990). While increments of the former characteristic stress are related to slip increments by a diagonal hardening matrix, as in Bassani and Wu's theory (Bassani and Wu 1989), increments in the latter are governed by an off-diagonally dominant hardening matrix, as in the formulation of Pierce and co-workers (1983).

Next we review some selected computational methods for the analysis of ductile single crystals. Our discussion emphasizes implicit integration and adaptive meshing techniques. A different and complementary perspective can be found in the earlier review article of Needleman *et al* (1985). More specifically, we consider state updates defined *à la* backward-Euler, and enforce global equilibrium and compatibility exactly at the end of each time step. It bears emphasis that the finite deformation aspects of the formulation, such as the finite rotations undergone by the lattice, are also treated exactly. We show that the state update can be reduced to a system of non-linear equations for the incremental slip strains. This system can be efficiently solved by means of a local Newton–Raphson iteration for which the Jacobian matrix can be written down explicitly. We also give an iterative procedure for identifying the active slip systems which reduces to the conventional elastic-predictor/plastic-corrector formulation of implicit updates for single-surface plasticity. An aspect of crystal plasticity models which is particularly attractive from the standpoint of implicit integration is that the *consistent* tangent moduli required to formulate a global Newton–Raphson solution procedure can be written down explicitly with some generality. This speeds up the computations by ensuring asymptotically quadratic convergence of the equilibrium iterations.

Because of the crystallographic nature of slip in single crystals, plastic flow is often confined to narrow regions across which displacements and stresses vary rapidly. In cases where the geometry of the slip patterns is not known *a priori*, adaptive meshing techniques furnish an effective means of resolving the fine structure of the solution. Despite its obvious

appeal, adaptive refinement has not been widely used in single-crystal calculations. General meshing techniques and state transfer operators which are applicable to finitely deforming plastic solids have been developed by Ortiz and Quigley (1991). Here we adapt these techniques to applications concerned with cracks in single crystals. An adaptation criterion based on the equidistribution of plastic work has been found effective for tracking and resolving the intricate slip patterns which arise in those applications.

The paper is organized as follows. Following some background on the general form of the constitutive relations for ductile crystals covered in section 2, hardening relations are discussed in sections 3 to 5, with special emphasis on dislocation models. Numerical matters related to constitutive updates and their integration into implicit solution procedures are taken up in section 6. In section 7, detailed comparisons with experiment are presented which demonstrate the ability of the theory to capture key features of the experimental record such as: latent hardening variations between secondary systems; variations of the onset and extent of the stages I and II of hardening with the orientation of the loading axis; patterns of slip activity; the evolution of dislocation densities, and others. As an example of application, in sections 8 and 9 we present calculations of the near-tip fields of a crack in a copper single crystal. The calculations are based on the dislocation model developed in the preceding sections. The numerical results are compared to the small-strain analytical solutions of Rice (1987) and Saaedvafa and Rice (1989) and to the previous calculations of Mohan and co-workers (1992a,b) for Al–Cu and Fe–Si alloys. The structure of the solution is seen to depend critically on the details of the hardening law and the assumed kinematics, which illustrates the need for physically based constitutive relations finely tuned to specific classes of crystals.

2. General constitutive framework

2.1. Incremental field equations

Consider a solid initially occupying a reference configuration B_0, and a process of incremental loading whereby the deformation mapping over B_0 changes from ϕ_n, at time t_n, to $\phi_{n+1} = \phi_n + \boldsymbol{u}$, at time $t_{n+1} = t_n + \Delta t$. We enforce equilibrium at time t_{n+1} weakly by recourse to the virtual work principle

$$\int_{B_0} \boldsymbol{P}_{n+1} : \nabla_0 \eta \, \mathrm{d}V_0 - \int_{B_0} \boldsymbol{f}_{n+1} \cdot \eta \, \mathrm{d}V_0 - \int_{\partial B_{0t}} \boldsymbol{t}_{n+1} \cdot \eta \, \mathrm{d}S_0 = 0 \tag{1}$$

where $\boldsymbol{P}_{n+1}$ denotes the first Piola–Kirchhoff stress field at time t_{n+1}, $\boldsymbol{f}_{n+1}$ and $\boldsymbol{t}_{n+1}$ are the corresponding body forces and boundary tractions, respectively, η is an admissible virtual displacement field, and ∇_0 denotes the material gradient. Assume for now that we have determined a rule to update the stress field of the general form

$$\boldsymbol{P}_{n+1} = \hat{\boldsymbol{P}}\left(\boldsymbol{F}_{n+1};\ \text{state at } t_n,\ \Delta t\right) \tag{2}$$

where the deformation gradients

$$\boldsymbol{F}_{n+1} = \nabla_0 \phi_{n+1} \tag{3}$$

are assumed given. Inserting (3) and (2) into (1) one obtains

$$\int_{B_0} \hat{\boldsymbol{P}}(\nabla_0 \phi_{n+1};\ \text{state at } t_n,\ \Delta t) : \nabla_0 \eta \, \mathrm{d}V_0 - \int_{B_0} \boldsymbol{f}_{n+1} \cdot \eta \, \mathrm{d}V_0 - \int_{\partial B_{0t}} \boldsymbol{t}_{n+1} \cdot \eta \, \mathrm{d}S_0 = 0 \tag{4}$$

which defines a set of non-linear equations which can be solved for the updated deformation mapping ϕ_{n+1}.

2.2. *General constitutive framework*

The total deformation of a crystal is the result of two main mechanisms: dislocation motion within the active slip systems and lattice distortion. Following Lee (1969), this points to a multiplicative decomposition

$$\boldsymbol{F} = \boldsymbol{F}^{\mathrm{e}}\boldsymbol{F}^{\mathrm{p}} \tag{5}$$

of the deformation gradient $\boldsymbol{F}$ into a plastic part $\boldsymbol{F}^{\mathrm{p}}$, defined as the cumulative effect of dislocation motion, and an elastic part $\boldsymbol{F}^{\mathrm{e}}$, which describes the distortion of the lattice. Following Teodosiu (1970) and others (Asaro and Rice 1977, Havner 1973, Hill and Rice 1972, Mandel 1972, Rice 1971) we shall assume that $\boldsymbol{F}^{\mathrm{p}}$ leaves the crystal lattice not only essentially undistorted, but also unrotated. Thus, the rotation of the lattice is contained in $\boldsymbol{F}^{\mathrm{e}}$. This choice of kinematics uniquely determines the decomposition (5). By virtue of (5), the deformation power per unit undeformed volume takes the form

$$\boldsymbol{P} : \dot{\boldsymbol{F}} = \bar{\boldsymbol{P}} : \dot{\boldsymbol{F}}^{\mathrm{e}} + \bar{\boldsymbol{\Sigma}} : \bar{\boldsymbol{L}}^{\mathrm{p}} \tag{6}$$

where

$$\bar{\boldsymbol{P}} = \boldsymbol{P}\boldsymbol{F}^{\mathrm{p}T} \qquad \bar{\boldsymbol{\Sigma}} = \boldsymbol{F}^{\mathrm{e}T}\boldsymbol{P}\boldsymbol{F}^{\mathrm{p}T} \qquad \bar{\boldsymbol{L}}^{\mathrm{p}} = \dot{\boldsymbol{F}}^{\mathrm{p}}\boldsymbol{F}^{\mathrm{p}-1} \tag{7}$$

Here, $\bar{\boldsymbol{P}}$ defines a first Piola–Kirchhoff stress tensor relative to the intermediate configuration $\bar{\mathcal{B}}_t$, and $\bar{\boldsymbol{\Sigma}}$ a stress measure conjugate to the plastic velocity gradients $\bar{\boldsymbol{L}}^{\mathrm{p}}$ on $\bar{\mathcal{B}}_t$, (Mandel 1972). The work conjugacy relations expressed in (6) suggest plastic flow rules and elastic stress–strain relations of the general form

$$\bar{\boldsymbol{L}}^{\mathrm{p}} = \bar{\boldsymbol{L}}^{\mathrm{p}}(\bar{\boldsymbol{\Sigma}}, \bar{\boldsymbol{Q}}) \tag{8a}$$

$$\bar{\boldsymbol{P}} = \bar{\boldsymbol{P}}(\boldsymbol{F}^{\mathrm{e}}, \bar{\boldsymbol{Q}}) \tag{8b}$$

Here, $\bar{\boldsymbol{Q}}$ denotes some suitable set of internal variables defined on the intermediate configuration, for which equations of evolution, or hardening laws, are to be supplied. A standard exercise shows that the most general form of (8*b*) consistent with the principle of material frame indifference is

$$\bar{\boldsymbol{P}} = \boldsymbol{F}^{\mathrm{e}}\bar{\boldsymbol{S}}(\bar{\boldsymbol{C}}^{\mathrm{e}}) \qquad \bar{\boldsymbol{C}}^{\mathrm{e}} = \boldsymbol{F}^{\mathrm{e}T}\boldsymbol{F}^{\mathrm{e}} \tag{9}$$

where $\bar{\boldsymbol{S}} = \bar{\boldsymbol{C}}^{\mathrm{e}-1}\bar{\boldsymbol{\Sigma}}$ is a symmetric second Piola–Kirchhoff stress tensor relative to the intermediate configuration $\bar{\mathcal{B}}_t$, and $\bar{\boldsymbol{C}}^{\mathrm{e}}$ is the elastic right Cauchy–Green deformation tensor on $\bar{\mathcal{B}}_t$. For most applications involving metals, a linear (but anisotropic) relation between $\bar{\boldsymbol{S}}$ and the elastic lagrangean strain $\bar{\boldsymbol{E}}^{\mathrm{e}} = (\bar{\boldsymbol{C}}^{\mathrm{e}} - \boldsymbol{I})/2$ can be assumed without much loss of generality. Higher-order moduli are given by Teodosiu (1982).

From the kinematics of dislocation motion, Rice (1971) showed that (8*a*) is of the form

$$\bar{\boldsymbol{L}}^{\mathrm{p}} = \sum_{\alpha} \dot{\gamma}^{\alpha} \bar{\boldsymbol{s}}^{\alpha} \otimes \bar{\boldsymbol{m}}^{\alpha} \tag{10}$$

where $\dot{\gamma}^\alpha$ is the shear rate on slip system α and $\bar{s}^\alpha$ and $\bar{m}^\alpha$ are the corresponding slip direction and slip plane normal. At this point the assumption is commonly made that $\dot{\gamma}^\alpha$ depends on stress only through the corresponding resolved shear stress τ^α, i.e.

$$\dot{\gamma}^\alpha = \dot{\gamma}^\alpha(\tau^\alpha, \bar{Q}) \tag{11}$$

which is an extension of Schmid's rule. If (11) is assumed to hold, then it was shown by Rice (1970) and by Mandel (1972) that the flow rule (10) derives from a viscoplastic potential.

The above constitutive framework for crystalline plasticity, or a close variant of it, has been used widely in the past. Some authors prefer to express the elastic response (9) in rate form. Computing the material time derivative of (9) and expressing the result in terms of spatial quantities leads to

$$L^e\tau = C^e d^e \tag{12}$$

where τ is the Kirchhoff stress, C^e are the (deformation dependent) elastic tangent moduli, d^e is the elastic rate of deformation tensor given by

$$d^e = (l^e + l^{eT})/2 \qquad l^e = \dot{F}^e F^{e-1} \tag{13}$$

and

$$L^e\tau = \dot{\tau} - l^e\tau - \tau l^{eT} \tag{14}$$

is the elastic Lie derivative of τ (for a formal definition of Lie derivative, see Marsden and Hughes (1983)). Because $l^e = d^e + w^e$, (12) can be rewritten by dropping the symmetric component of l^e in the elastic Lie derivative of τ, which thus reduces to the elastic Jaumann rate of τ (Hill and Rice 1972), and absorbing the coefficients of that symmetric part into redefined moduli C^e having the same symmetries as the original ones. As a simplification, the moduli C^e are sometimes taken to be constant, despite the fact that this choice is inconsistent with hyperelasticity (Simó and Pister 1984). For metals, these variations of the theory have a negligible effect on the outcome of the computations.

In order to complete the constitutive description of the crystal, hardening relations governing the evolution of the internal variables $\bar{Q}$ need to be provided. By way of example, we next outline two models which are illustrative of a phenomenological framework commonly adopted in numerical simulations.

2.3. The model of Pierce, Asaro and Needleman (1983)

Pierce and co-workers (1983) developed a phenomenological crystal plasticity model which has been widely used in computation. The rate of shear deformation on slip system α is given by a power-law of the form

$$\dot{\gamma}^\alpha = \begin{cases} \dot{\gamma}_0(\tau^\alpha/g^\alpha)^{1/m} & \text{if } \tau^\alpha \geqslant 0 \\ 0 & \text{otherwise.} \end{cases} \tag{15}$$

Here, m is the strain-rate sensitivity exponent, $\dot{\gamma}_0$ is a reference shear strain rate, and g^α is the current shear flow stress on slip system α. It should be carefully noted that implicit in the form in which (15) is written is the convention of differentiating between the positive

and negative slip directions $\pm\bar{m}^\alpha$ for each slip system, whereupon the slip rates $\dot{\gamma}^\alpha$ can be constrained to be non-negative.

The set of internal variables $\bar{Q}$ is identified with $\{g^\alpha, \gamma^\alpha\}$. For multiple slip, the evolution of the flow stresses is taken to be governed by the hardening law

$$\dot{g}^\alpha = \sum_\beta h^{\alpha\beta}\dot{\gamma}^\beta \tag{16}$$

where $h^{\alpha\beta}$ are the hardening moduli. These are assumed to be of the form

$$h^{\alpha\beta} = h(\gamma)\left[q + (1-q)\delta^{\alpha\beta}\right] \tag{17}$$

where $\gamma = \sum_\alpha \gamma_\alpha$ is the sum of the slip strains on all slip systems. The parameter q characterizes the hardening behavior. The choice $q = 1$ corresponds to isotropic or Taylor hardening. For FCC metals, Kocks (1970) determined experimentally the range of this parameter to be $1 \leqslant q \leqslant 1.4$. It bears emphasis that, in the latent hardening experiments of Kocks (1970), the flow stresses were measured by back-extrapolation.

A form of $h(\gamma)$ in (17) appropriate to Al–Cu alloys is (Chang and Asaro, 1981)

$$h(\gamma) = h_0 \operatorname{sech}^2[h_0\gamma/(\tau_s - \tau_0)] \tag{18}$$

where h_0 is the initial hardening rate, τ_0 is the critical resolved shear stress and τ_s is the saturation strength. Comparisons between (18) and experimental data are given by Asaro (1983).

2.4. *The model of Bassani and Wu (1989)*

Based on carefully controlled latent hardening experiments in copper single crystals (Wu *et al* 1989), Bassani and Wu (1989) (see also Bassani 1990) have recently proposed a model of hardening in single crystals in which the hardening moduli are taken to be of the form

$$\begin{aligned} h_{\alpha\alpha} &= \left[(h_0 - h_s)\operatorname{sech}^2\left(\frac{(h_0 - h_s)\gamma_\alpha}{\tau_1 - \tau_0}\right) + h_s\right]\left[1 + \sum_{\beta\neq\alpha} f_{\alpha\beta}\tanh\left(\frac{\gamma_\beta}{\gamma_0}\right)\right] \\ h_{\alpha\beta} &= \epsilon h_{\alpha\alpha} \end{aligned} \tag{19}$$

where τ_1 is the stage I stress, i.e. the breakthrough stress at which large plastic flow initiates, h_0 and h_s define the hardening slope immediately following initial yield and during easy glide, respectively, and ϵ is a small parameter which defines the off-diagonal terms. Following Franciosi and co-workers (Franciosi *et al* 1980, Franciosi and Zaoui 1982, Franciosi 1983, 1985a,b, 1988), the amplitude factors $f_{\alpha\beta}$ are taken to depend on the type of dislocation junction formed between α and β slip systems. They are classified into four groups and are represented by four constants (cf section 4). The article of Bassani and Wu (1989) may be consulted for further details.

A noteworthy feature of the hardening matrix (19) is that, contrary to the form (17) assumed by Pierce and co-workers (1983), it is diagonally dominant. We return to this question in section 5, where we show how these discrepancies can easily be reconciled.

3. Self-hardening

Next we endeavor to derive the hardening relations of ductile crystals from dislocation mechanics. We begin by considering the motion of dislocations within a generic slip system. For simplicity of notation, throughout this section we shall omit the label α identifying the specific slip system under consideration. This motion is the result of the intricate interplay between moving dislocations, which are driven by the resolved shear stress acting on the slip system, and obstacles. The central assumption in the forest theory of hardening is that, for high-purity single-phase crystals, the main resistance to dislocation motion is posed by secondary dislocations piercing the slip plane, or forest dislocations. Detailed numerical simulations of a dislocation line propagating though forest dislocations have been carried out by Foreman and Makin (1966, 1967), and by Kocks (1966), but a complete analytical treatment was lacking. Because of the random nature of the interactions, the motion of dislocations through a distribution of obstacles is best described in statistical terms. Here we closely follow the statistical mechanical theory proposed by Ortiz and Popov (1982).

3.1. Distribution of obstacle strengths

Forest dislocations are non-extended obstacles whose interactions are effective over a few atomic distances only, and can therefore be idealized as point obstacles. Pairs of such point obstacles arrest dislocations, which require a certain threshold resolved shear stress s to overcome the barrier (see figure 1). The value of s can be estimated from line tension calculations, see for example Kovács and Zsoldos (1973). The simplest such estimate gives

$$s = \alpha\mu b/l \tag{20}$$

where μ is the shear modulus, b the length of the Burgers vector, l the length of the link, and α a numerical coefficient of the order of 0.3 (Kuhlmann–Wilsdorf 1989). For simplicity, we start by assuming that all forest dislocation intersections give rise to obstacles of the same strength, regardless of the precise nature of the interaction. This assumption is relaxed in section 4.

Since the distribution of point obstacles within the glide plane is random, it follows that s itself is a random variable. We shall let $\tilde{f}(s,t)$ denote the probability density function of two-point barrier strengths at time t. The time dependence of $\tilde{f}(s,t)$ is a consequence of the variation in forest dislocation density. If, for simplicity, the locations of the point obstacles are assumed to be completely uncorrelated, and assuming further that the pairs of points defining a barrier are nearest neighbours, it follows that (Kocks 1966)

$$\tilde{f}(l,t) = 2\pi n(t) l \ \exp\left[-\pi n(t) l^2\right] \tag{21}$$

where $n(t)$ is the area density of forest dislocation intersections with the glide plane at time t, and $\tilde{f}(l,t)$ is the probability density function for nearest neighbour distances. Using (20) to effect a change of variables from l to s, we arrive at

$$\tilde{f}(s,t) = \left[2\pi n(t)(\alpha\mu b)^2/s^3\right] \exp\left[-\pi n(t)\left(\alpha\mu b/s\right)^2\right]. \tag{22}$$

The corresponding distribution function is computed to be

$$\tilde{P}(s,t) = \exp\left[-\pi n(t)\left(\alpha\mu b/s\right)^2\right]. \tag{23}$$

Direct measurements of $\tilde{f}(l,t)$ were made by Mughrabi (1975), and by Grosskreutz and Mughrabi (1975). The ability of (21) to fit the data is quite remarkable.

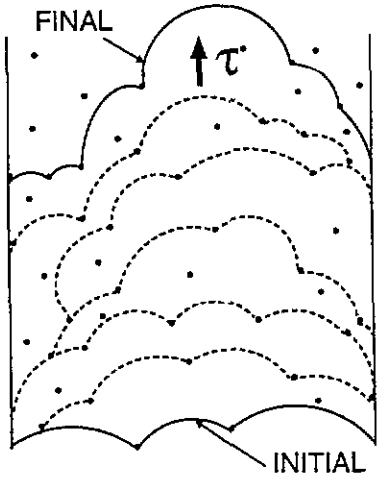

Figure 1. Schematic representation of a dislocation passing through a random distribution of point obstacles under the action of a monotonically increasing resolved shear stress τ.

3.2. Kinetics of dislocation motion

Next we turn to the interaction between a moving dislocation line and the distribution of point obstacles. Our discussion here is restricted to the analytically tractable case of rate-independent behavior and monotonic loading. A more general theory which accounts for rate-sensitivity effects and arbitrary loading paths has been given by Ortiz and Popov (1982). Thermal effects can be included in the theory by recourse to models of thermally activated dislocation motion such as those advanced by Teodosiu and Sidoroff (1976).

Let $\tau(t)$ be the resolved shear stress acting on the slip system at time t. Assume for now that $\tau(t)$ increases monotonically from zero at $t = 0$. Evidently, for dislocations to be stable at time t they must face barriers of strengths s in excess of $\tau(t)$. As $\tau(t)$ is increased to $\tau(t) + \dot{\tau}(t)\,dt$, the dislocation segments held at barriers of strengths in the range $\tau(t) \leqslant s \leqslant \tau(t) + \dot{\tau}(t)\,dt$ are dislodged and move forward until they reach barriers of strength $s \geqslant \tau(t) + \dot{\tau}(t)\,dt$ (figure 1). This motion of dislocations results in an incremental increase in the plastic deformation. In the rate-independent formulation, the dislocation jumps between obstacles are assumed to be instantaneous. This idealization is justified for quasistatic loading, when the duration of the flights is much smaller than the characteristic time of variation of the loads.

As noted by Ortiz and Popov (1982), the information needed to describe the dislocation motion is fully contained in the probability density function $f(s,t)$, which represents the fraction of dislocation length facing barriers of strength s at time t. This is, therefore, the primary unknown of the theory. The function $f(s,t)$ evolves in time due to the process of redistribution of dislocation line described above. Initially, though, the dislocations may be assumed to be randomly distributed over their slip plane, and

$$f(s,0) = \tilde{f}(s,0). \tag{24}$$

At later times, $f(s,t)$ must vanish identically for $0 \leqslant s < \tau(t)$ in the rate-independent limit.

Next, we endeavor to determine a kinetic equation for the evolution of $f(s,t)$. Consider a time increment dt over which the applied resolved shear stress is incremented by an amount

$\dot{\tau}(t)\,\mathrm{d}t$, with $\dot{\tau}(t) \geqslant 0$. Then, the dislocation segments facing barriers of strengths in the interval $\tau(t) \leqslant s \leqslant \tau(t)+\dot{\tau}(t)\,\mathrm{d}t$ become unstable and move to stronger barriers of strengths $s > \tau(t) + \dot{\tau}(t)\,\mathrm{d}t$. The probability that an unstable dislocation segment moves to a barrier of strength s' is given by

$$\tilde{f}[s'|s' > \tau(t)] = \frac{\tilde{f}(s', t)H[(s' - \tau(t)]}{1 - \tilde{P}[\tau(t), t]} \tag{25}$$

where H is the Heaviside step function. Thus, the displaced dislocation segments redistribute themselves proportionally to $\tilde{f}(s', t)$ over the admissible interval $[\tau(t), \infty)$. Consequently, the transition probability that a dislocation segment moves from a barrier of strength s to another of strength s' is $\tilde{f}[s'|s' > \tau(t)]\delta[s - \tau(t)]\dot{\tau}(t)\,\mathrm{d}t$, and the correponding transition probability rate is

$$\psi(s \to s', t) = \frac{\tilde{f}(s', t)H[s' - \tau(t)]}{1 - \tilde{P}[\tau(t), t]}\delta[s - \tau(t)]\dot{\tau}(t). \tag{26}$$

Because of the Markovian nature of the dislocation flights, the evolution of $f(s, t)$ is governed by Pauli's master equation (see, e.g. Résibois and de Leener 1977)

$$\frac{\partial f(s, t)}{\partial t} = \int_0^\infty [\psi(s' \to s, t)f(s', t) - \psi(s \to s', t)f(s, t)]\,\mathrm{d}s' + g(s, t) \tag{27}$$

where $g(s, t)$ is a source term which describes the rate of variation of $f(s, t)$ due to external agencies and in the absence of transitions. For the system under consideration, $g(s, t)$ represents the rate of change of $f(s, t)$ due to the evolution of barrier strength probabilities $\tilde{f}(s, t)$. As noted earlier, this latter evolution is in turn caused by variations in the density of forest dislocations $n(t)$, e.g. through (22).

To evaluate $g(s, t)$ we view $\tau(t)$ as frozen at its current value and suppose that $\tilde{f}(s, t)$ changes into $\tilde{f}(s, t + \mathrm{d}t)$, i.e. we regard all dislocation segments as stably pinned at their current locations, while point obstacles are added or removed from the slip plane. Some of the new obstacles pin down the dislocation lines and, consequently, a change in $f(s, t)$ results. The probability that a segment comes to face a newly formed barrier of strength s is proportional to $\tilde{f}(s, t)$, over the admissible range $[\tau(t), \infty)$. Therefore, the rate at which $f(s, t)$ changes due to this mechanism is

$$g(s, t) = (\partial/\partial t)\Big[\{\tilde{f}(\tau, t)/[1 - \tilde{P}(\tau, t)]\}H(s - \tau)\Big]_{\tau=\tau(t)} \tag{28}$$

where the notation implies that the time derivative is to be carried out at constant τ.

Inserting (26) and (28) into (27) the sought equation of evolution for $f(s, t)$ is found to be

$$\begin{aligned}\partial f(s, t)/\partial t = &\Big[\tilde{f}(s, t)H[s - \tau(t)]/\{1 - \tilde{P}[\tau(t), t]\} - \delta[s - \tau(t)]\Big]f[\tau(t), t]\dot{\tau}(t) \\ &+ (\partial/\partial t)\Big[\{\tilde{f}(\tau, t)/[1 - \tilde{P}(\tau, t)]\}H(s - \tau)\Big]_{\tau=\tau(t)}\end{aligned} \tag{29}$$

where it is implicitly understood that $\dot{\tau}(t) \geqslant 0$.

Equation (29) may be viewed as a statement of gains and losses. Indeed, the Dirac-delta term on the right hand side has the effect of removing probability density from the interval

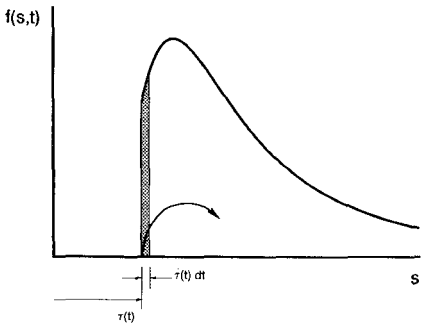

Figure 2. Redistribution of the probability density $f(s, t)$ upon a resolved shear stress increment $\dot{\tau}(t)\,\mathrm{d}t$.

$\tau(t) \leqslant s \leqslant \tau(t) + \dot{\tau}(t)\,\mathrm{d}t$, while the remaining term in the bracket distributes it over the admissible interval $[\tau(t), \infty)$ proportionally to $\tilde{f}(s, t)$ (figure 2).

The third term represents a probability source term, as discussed in the foregoing. We note that

$$\int_0^\infty \frac{\partial f(s,t)}{\partial t}\,\mathrm{d}s = 0 \tag{30}$$

which, together with (24), insures that the normalization condition

$$\int_0^\infty f(s,t)\,\mathrm{d}s = 1 \tag{31}$$

is satisfied at all times. A noteworthy limiting case of (29) is obtained when $\tau(t) = 0$, $t \geqslant 0$, i.e. when the slip system remains unloaded at all times. In this case, it follows immediately from (29) that $f(s, t) = \tilde{f}(s, t)$, $t \geqslant 0$. That this should indeed be the case follows from the fact that, in the absence of applied stress, the dislocation lines remain randomly distributed over the slip plane and, consequently, the probability that a segment face a barrier of strength s is necessarily equal to $\tilde{f}(s, t)$.

Remarkably, kinetic equation (29) admits the simple closed form solution

$$f(s,t) = \frac{\tilde{f}(s,t)H[s-\tau(t)]}{1-\tilde{P}[\tau(t),t]}. \tag{32}$$

This probability density function is readily verified to satisfy (29) by direct substitution. Again, it should be emphasized that (32) is valid for monotonically increasing $\tau(t)$ only. The case of general loading is considerably more complex (Ortiz and Popov 1982). Solution (32) implies that, under the conditions of the analysis, the probability density $f(s, t)$ remains proportional to $\tilde{f}(s, t)$ over the current admissible range $[\tau(t), \infty)$. The various stages of the evolution of $f(s, t)$ are shown in figure 3, for the case in which $\tilde{f}(s, t)$ and $\tilde{P}(s, t)$ are given by (22) and (23), respectively. As will be demonstrated subsequently, (32) fully characterizes the self-hardening of a slip system.

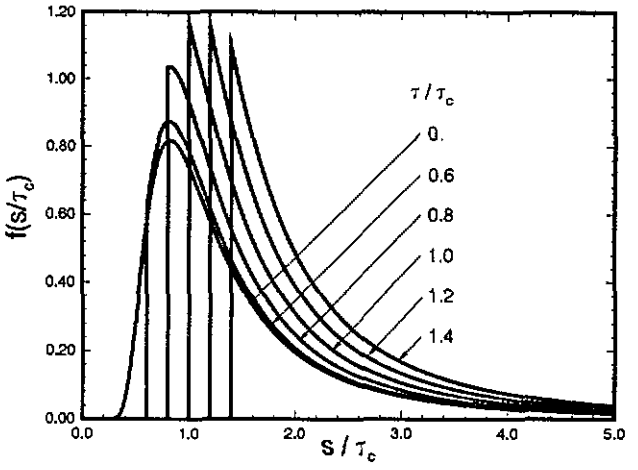

Figure 3. Probability density $f(s, t)$ for different values of τ/τ_c.

3.3. Plastic strain rate

Next we proceed to calculate the slip rate $\dot{\gamma}(t)$ induced by the dislocation motion. Let $\rho(t)$ denote the current dislocation length per unit volume for the slip system under consideration. $\rho(t)$ varies in time according to kinetic equations formulated in section 4. The dislocation density released during an increment of the resolved shear stress from $\tau(t)$ to $\tau(t) + \dot{\tau}(t)\,dt$ gives rise to an incremental plastic strain (Kocks 1966, Teodosiu 1970)

$$d\gamma(t) = b\rho(t) f[\tau(t), t]\dot{\tau}(t)\,dt\bar{N}(t)\bar{l}(t) \tag{33}$$

where $\bar{l}(t)$ is the average distance between barriers, and $\bar{N}(t)$ is the average number of jumps the dislocation segments make before attaining stable positions (figure 4).

To a good approximation, $\bar{l}(t)$ can be identified with the average distance $\langle l\rangle(t)$ between point obstacles. For $f(l, t)$ as in (21), this gives

$$\bar{l}(t) = \langle l\rangle(t) = 1/2\sqrt{n(t)}. \tag{34}$$

Next we compute the average number of jumps $\bar{N}(t)$. Evidently, the probability that an unstable segment becomes arrested after the first jump is equal to the probability that the first barrier encountered is of a strength $s \geqslant \tau(t)$. This probability is $1 - \tilde{P}[\tau(t), t]$. The probability that the segment goes beyond the first barrier is $\tilde{P}[\tau(t), t]$. Likewise, the probability that a segment gets arrested at the second barrier encountered is $\tilde{P}[\tau(t), t]\{1 - \tilde{P}[\tau(t), t]\}$, and the probability that it goes beyond is $\tilde{P}^2[\tau(t), t]$, and so on. Hence, the average number of jumps between barriers taken by an unstable segment is

$$\begin{aligned}\bar{N}(t) &= \{1 - \tilde{P}[\tau(t), t]\} + 2\tilde{P}[\tau(t), t]\{1 - \tilde{P}[\tau(t), t]\} + 3\tilde{P}^2[\tau(t), t]\{1 - \tilde{P}[\tau(t), t]\} \\ &= 1/\{1 - \tilde{P}[\tau(t), t]\}.\end{aligned} \tag{35}$$

Interestingly, if $\tau = 0$, any moving dislocation segment is sure to be arrested at the first obstacle it encounters, and $\bar{N} = 1$, in agreement with (35). Likewise, if $\tilde{f}(s, t)$ has a

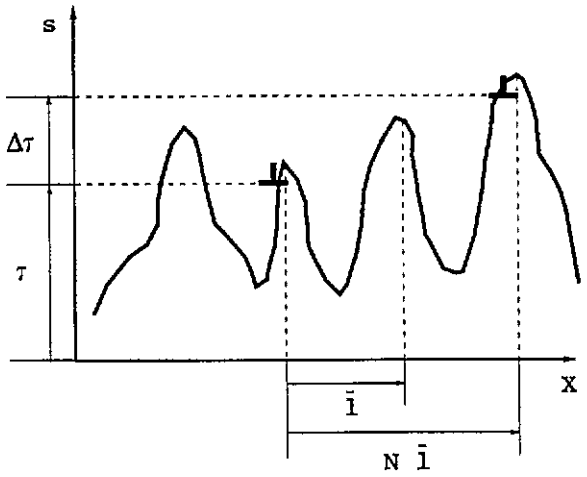

Figure 4. 1D schematic representation of a dislocation segment moving through random obstacles. The dislocation segment is initially trapped at an obstacle of strength $s \geqslant \tau$. After a resolved shear stress increment $\Delta\tau$ is applied, the segment glides until it is trapped again at a new obstacle of strength $s \geqslant \tau + \Delta\tau$.

bounded support, say $[0, s_{\max}(t)]$, and $\tau(t) > s_{\max}(t)$, then the segment never reaches a stable barrier and $\bar{N} \to \infty$, as predicted by (35).

Substituting (35) and (32) with $s = \tau^+(t)$ into (33) we finally obtain

$$\dot{\gamma}(t) = \gamma_c(t)\frac{\tilde{f}[\tau(t), t]}{\{1 - \tilde{P}[\tau(t), t]\}^2}\dot{\tau}(t) \tag{36}$$

where the characteristic plastic strain $\gamma_c(t)$ is defined as

$$\gamma_c(t) = b\rho(t)\bar{l}(t). \tag{37}$$

It bears emphasis that (36) is explicit in $\tilde{f}(s, t)$ and $\rho(t)$. The former is given by (22) and (23), once the point obstacle density $n(t)$ is known. This, in turn, is a function of the dislocation densities in the remaining slip systems. The precise form of this dependence is discussed in section 4.

3.4. Self-hardening

As expected from the rate-independent character of the formulation, (36) defines a relation of the form

$$\dot{\gamma}(t) = \dot{\tau}(t)/h(t) \tag{38}$$

where $h(t)$ is the self-hardening modulus of the slip system. In view of (36) one has, explicitly,

$$1/h(t) = \gamma_c(t)\frac{\tilde{f}[\tau(t), t]}{\{1 - \tilde{P}[\tau(t), t]\}^2}. \tag{39}$$

As before, this formula is valid for any assumed distribution $\tilde{f}(s,t)$ of barrier strengths. If, for instance, we take $\tilde{f}(s,t)$ to be given by (22), then (39) becomes

$$h(t) = h_c(t)\left[2\tau^3(t)/\tau_c^3(t)\right]\left\{\cosh\left[\tau_c^2(t)/\tau^2(t)\right] - 1\right\} \tag{40}$$

where

$$\tau_c(t) = \alpha\mu b\sqrt{\pi n(t)} \qquad h_c(t) = \tau_c(t)/\gamma_c(t) \tag{41}$$

are a characteristic shear stress and plastic modulus, respectively. Equation (40) predicts an initial infinite hardening modulus at $\tau = 0$. The hardening modulus subsequently decreases monotonically to zero as τ is increased. The values of τ_c and γ_c determine the location of the 'bend' in the resolved shear stress–slip strain curve. Thus, τ_c correlates with the value of the flow stress determined by back-extrapolation.

3.5. Elastic unloading and rate effects

In the present rate-independent framework, the above relations can be extended simply to account for loading histories exhibiting elastic unloading. Thus, we no longer assume that the loading is monotonic, but continue to require that $\tau(t)$ not change sign throughout the loading history. Define the current flow stress $g(t)$ of the slip system as

$$g(t) = \max_{s\in[0,t]} \tau(s). \tag{42}$$

In rate form

$$\dot{g}(t) = \begin{cases} \dot{\tau}(t) & \text{if } \tau(t) = g(t) \text{ and } \dot{\tau}(t) \geqslant 0 \\ 0 & \text{otherwise.} \end{cases} \tag{43}$$

Thus, $g(t)$ is defined to be the maximum attained resolved shear stress on the slip system.

Because $f(s,t)$ vanishes in the interval $[0, g(t)]$, it follows from (33) that $\dot{\gamma}(t) = 0$ if $\tau(t) < g(t)$. Thus, the interval $[0, g(t))$ acts as an induced elastic domain: any part of the loading history contained in $[0, g(t))$ leaves γ (and g) unchanged. The same is true of loading increments such that $\tau(t) = g(t)$ but $\dot{\tau}(t) = 0$. Note that in this latter case $\dot{g}(t) = 0$. Physically, the stability of the dislocations in the glide system requires that they all be pinned at obstacles of strength greater or equal to the previously maximum attained resolved shear stress $g(t)$. Therefore, subsequent stresses in the range $[0, g(t))$ are not capable of causing further dislocation motion. Under these conditions (38) and (39) are to be rewritten as

$$\dot{\gamma}(t) = \frac{\dot{g}(t)}{h(t)} \qquad \frac{1}{h(t)} = \gamma_c(t)\frac{\tilde{f}[g(t),t]}{\{1 - \tilde{P}[g(t),t]\}^2}. \tag{44}$$

It is evident from (43) that the first of (44) incorporates the loading–unloading criteria appropriate to non-monotonic loading.

The preceding analysis can be generalized to the case in which the dislocation jumps between obstacles are not instantaneous but occur at a speed which is a function of the resolved shear stress (Ortiz and Popov 1982). Unfortunately, the resulting master equation (27) cannot be solved in closed form. Phenomenologically, however, rate effects can be readily built into the constitutive description by adopting a power viscosity law of the form (15). Mathematically, the resulting formulation can be regarded as a viscoplastic regularization of the rate-independent relations.

4. Cross-hardening

The preceding section has been concerned with the statistics of the motion of a dislocation line through dislocations intersecting its plane, or forest dislocations. The ensuing short-range interactions determine the rate of self-hardening of a slip system in the present theory. A key variable in the description of the self-hardening of, say, system α is the density n^α of point obstacles afforded by forest dislocations. Evidently, n^α is a function of the dislocation densities in all remaining systems. The experimental work of Franciosi and co-workers (Franciosi *et al* 1980, Franciosi and Zaoui 1982, Franciosi 1983, 1985a,b, 1988) is suggestive of a dependence of the form

$$n^\alpha = \sum_\beta a^{\alpha\beta}\rho^\beta. \tag{45}$$

Experimentally determined values of the interaction matrix $a^{\alpha\beta}$ have been given by Franciosi and Zaoui (1982) for the twelve slip systems belonging to the family of {111} planes and [110] directions in FCC crystals, and by Franciosi (1983) for the twenty-four systems of types {211} [111] and {110} [111] in BCC crystals.

They classify the interactions according to whether the dislocations belong to the same system (interaction coefficient a_0), fail to form junctions (interaction coefficient a_1), form Hirth locks (interaction coefficient a_1), co-planar junctions (interaction coefficient a_1), glissile junctions (interaction coefficient a_2), or sessile Lomer–Cottrell locks (interaction coefficient a_3), with $a_0 \leqslant a_1 \leqslant a_2 \leqslant a_3$. Franciosi (1985) has also found the interaction coefficients to be linearly dependent on the stacking fault energy of the crystal, the degree of anisotropy increasing with decreasing stacking fault energy.

It bears emphasis that the statistical analysis given in section 3 is predicated on the simplifying assumption that all point obstacles on a slip plane are of equal strength. However, the strength of point obstacles, as measured by the coefficient α in (20), may be expected to be a strong function of the type of threading dislocation (Baird and Gale 1965). A rigorous treatment of obstacle strength distribution effects necessitates a substantial modification of the statistical analysis given in section 3 (see, e.g. Friedrichs and Haasen 1975). In a more phenomenological vein, it is possible to lump α and n together in equation (41) and account for obstacle strength variations through the coupling matrix $a^{\alpha\beta}$ following Franciosi.

In order to obtain a closed set of constitutive relations, equations of evolution for the dislocation densities are required. Processes resulting in changes in dislocation density include production by fixed sources, such as Frank–Read sources, breeding by cross-glide and pair annihilation (see Kuhlmann-Wilsdorf 1989, for a recent review). The operation of fixed Frank–Read sources, however, usually stops after inducing a relatively small amount of plastic deformation. Consequently, production by fixed sources, while sometimes important during the early stages of plastic deformation, is quickly eclipsed by production due to cross-glide and can be safely neglected.

The importance of breeding by cross-glide as a dislocation generation mechanism was emphasized by Johnston and Gilman (1959, 1960). In this mechanism, the screw section of a moving dislocation migrates to a parallel plane by cross-slip, thus creating a pair of immovable jogs. The ends of the jogs act as the fixed points of single-ended plane sources. Theoretical (Li 1961) and experimental (Johnston and Gilman 1959, 1960) investigations suggest that the breeding rate due to cross-glide is proportional to the mean dislocation speed. This gives the relation

$$b\dot{\rho}^\alpha = \lambda\dot{\gamma}^\alpha \tag{46}$$

for the rate of dislocation generation due to cross-glide multiplication. The coefficient λ may be interpreted as the reciprocal mean free path between cross-glide events. The rate of pair annihilation is proportional to the probability of having two dislocations segments of opposite sign within a small neighbourhood, and, thus, may be expected to be roughly proportional to the dislocation density squared (Sackett *et al* 1976). The average time between encounters is inversely proportional to the mean dislocation speed. Consequently, the rate of dislocation attrition due to pair annihilation can be expressed as (Sackett *et al* 1976)

$$b\dot{\rho}^{\alpha} = -\kappa\rho^{\alpha}\dot{\gamma}^{\alpha} \tag{47}$$

where κ may be regarded as the mean radius of interaction for segment annihilation.

Combining (46) and (47), the total rate of change of dislocation density may be written in the suggestive form (Gillis and Gilman 1965, Essmann and Rapp 1973)

$$\dot{\rho}^{\alpha} = (\lambda/b)\left(1 - \rho^{\alpha}/\rho^{\text{sat}}\right)\dot{\gamma}^{\alpha} \tag{48}$$

where $\rho^{\text{sat}} \equiv \lambda/\kappa$ is a saturation density at which the rate of annihilation balances the rate of production. Equation (48) defines a linear ordinary differential equation for ρ^{α} of solution

$$\rho^{\alpha} = \rho_{\text{sat}}\left[1 - \left(1 - \rho_0^{\alpha}/\rho_{\text{sat}}\right)\exp(-\gamma^{\alpha}/\gamma_{\text{sat}})\right] \tag{49}$$

where $\gamma_{\text{sat}} \equiv b\rho_{\text{sat}}/\lambda$ is a saturation shear strain, ρ_0^{α} is the initial dislocation density in system α, and we have assumed that $\gamma^{\alpha}(0) = 0$. It bears emphasis that relation (49) places the dislocation density ρ^{α} and the slip strain γ^{α} in one-to-one correspondence.

It should be carefully noted that we do not differentiate explicitly between mobile and immobile dislocation densities. In the above expressions, ρ^{α} is used to denote the total (i.e. mobile and immobile) dislocation density. At any time during the deformation process, the fraction of the dislocation density which contributes to the plastic strain rate $\dot{\gamma}^{\alpha}$ is determined by the probability density function $f(s, t)$ introduced in the preceding section. Since (48) involves $\dot{\gamma}^{\alpha}$, the right hand side is implicitly proportional to the mobile dislocation fraction.

5. Summary of constitutive relations

For ease of reference, the relations defining the dislocation model are collected in box 1. Remarkably, the dislocation-based model outlined in box 1 conforms to the general structure suggested by Bassani and Wu (1989) on the basis of their own experimental data. Specifically, the matrix $h^{\alpha\beta}$ entering the hardening relations (16) is predicted to be *diagonal*. The precise way in which latent hardening is predicted to occur by the dislocation model is as follows. During the initial single-slip regime, dislocation multiplication takes place predominantly on the primary slip system. Hence, the number of point obstacles on the primary system remains relatively small (constant if $a^{\alpha\alpha} = 0$) and the deformation proceeds by easy glide. At the same time, the number of point obstacles on the secondary systems grows rapidly due to dislocation multiplication on the primary system, with rates determined by the influence coefficients $a^{\alpha\beta}$. This has the effect of raising the values of the reference, or 'critical', stresses τ_c^{β} on the secondary systems. Consequently, despite the fact that the yield stress g^{β} remains small on the secondary systems, the reloading curve in a latent-hardening experiment simulation rises steeply above the primary loading curve,

as observed experimentally (e.g. Kocks, 1970). A detailed comparison between theory and latent-hardening data is presented in section 7.2.

Box 1. Hardening relations

$$\dot{\gamma}^\alpha \equiv \phi(\tau^\alpha, g^\alpha) = \begin{cases} \dot{\gamma}_0\left[(\tau^\alpha/g^\alpha)^{1/m} - 1\right] & \text{if } \tau^\alpha > g^\alpha; \\ 0, & \text{otherwise.} \end{cases}$$

$$\dot{g}^\alpha = h^{\alpha\alpha}\dot{\gamma}^\alpha$$

$$h^{\alpha\alpha} = h_c^\alpha \left(\frac{g^\alpha}{\tau_c^\alpha}\right)^3 \left\{\cosh\left[\left(\frac{\tau_c^\alpha}{g^\alpha}\right)^2\right] - 1\right\}$$

$$h_c^\alpha = \frac{\tau_c^\alpha}{\gamma_c^\alpha}, \qquad \tau_c^\alpha \equiv \alpha\mu b\sqrt{\pi n^\alpha}, \qquad \gamma_c^\alpha \equiv \frac{b\rho^\alpha}{2\sqrt{n^\alpha}}$$

$$n^\alpha = \sum_\beta a^{\alpha\beta}\rho^\beta$$

$$\rho^\alpha = \rho_{\text{sat}}\left[1 - \left(1 - \frac{\rho_0}{\rho_{\text{sat}}}\right)e^{-\gamma^\alpha/\gamma_{\text{sat}}}\right]$$

The correspondence between the dislocation model and that of Pierce and co-workers (1983) can be made more apparent by computing $\dot{\tau}_c^\alpha$ from (41), (45) and (48). As noted earlier, τ_c^α correlates with the flow stress obtained by back-extrapolation. A simple calculation shows that $\dot{\tau}_c^\alpha$ and $\dot{\gamma}^\beta$ are linearly related as

$$\dot{\tau}_c^\alpha = \sum_\beta \hat{h}^{\alpha\beta}\dot{\gamma}^\beta \qquad \hat{h}^{\alpha\beta} = (\tau_c^\alpha/2n^\alpha)a^{\alpha\beta}(\lambda/b)(1 - \rho^\beta/\rho^{\text{sat}}). \tag{50}$$

Evidently, the hardening matrix $\hat{h}^{\alpha\beta}$ is non-diagonal. Initially, when the dislocation densities are low on all systems, the ordering $a^{\alpha\beta} \gg a^{\alpha\alpha}$ results in the off-diagonal terms of $\hat{h}^{\alpha\beta}$ being dominant. It should be noted, however, that the hardening matrix $\hat{h}^{\alpha\beta}$ is not constant but depends strongly on the deformation history.

It may therefore be concluded that some of the discrepancies between the various theories regarding the form of the hardening matrix stem largely from the definition of flow stress adopted. If, as in the model of Pierce and co-workers, the emphasis is placed on τ_c^β, which roughly corresponds to a back-extrapolation definition of the flow stress as in Kocks (1970), then the corresponding hardening matrix is non-diagonal. If, on the other hand, the variation of the yield stress, or elastic limit, is sought, as in the model of Bassani and Wu (1989), then a diagonal hardening matrix becomes appropriate. The dislocation model outlined in the foregoing shows that these two views are complementary, rather than contradictory.

6. Numerical implementation

Next we turn our attention to matters of numerical implementation of the foregoing models in the context of implicit finite-element computation. Implicit finite-element methods applied

to elastoplastic solids can prove advantageous in applications in which the stress and deformation paths remain nearly proportional. Under these conditions, implicit methods can significantly speed up the calculations by enabling the use of larger time steps than otherwise permitted by their explicit counterparts. Even if the global equilibrium equations are handled explicitly, it is often advantageous to perform the local updates implicitly, since implicit updates add considerable robustness to the calculations and rid them of the exacting constraints placed by stability in the nearly rate-independent limit.

Implicit methods which seek to exactly satisfy equilibrium, compatibility and some suitable state-update rule at every load increment were formalized by Hughes and Taylor (1978) for the viscoplastic solid, and by Simó and Taylor (1985) for the rate-independent solid. A Newton–Raphson solution of the resulting incremental non-linear equations requires the formulation of so-called 'consistent tangents' (Simó and Taylor 1985) obtained by direct linearization of the state-update algorithm. Here we focus on the backward-Euler or fully implicit method and show how the local update can be reduced to a non-linear system of equations for the incremental slip strains. The Jacobian matrix of the system can be derived explicitly, which enables the efficient computation of the incremental slip strains by a local Newton–Raphson iteration. We also give the consistent tangents for the algorithm explicitly in closed form. A difficulty which arises in the context of crystalline plasticity concerns the determination of the active slip systems under conditions of multiple slip. We define an iterative procedure for determining the pattern of slip activity which reduces to the conventional elastic-predictor plastic-corrector implementation of implicit updates for solids with a single yield surface.

6.1. Consistent tangents

In a Newton–Raphson solution of the governing equations (4), the linearized problem for the incremental displacements takes the form

$$\int_{B_0} \nabla_0 \boldsymbol{\eta} : \hat{\boldsymbol{K}}_{n+1} : \nabla_0 \boldsymbol{u} \, \mathrm{d}V_0 - \text{forcing terms} = 0 \tag{51}$$

where the 'consistent tangents' $\hat{\boldsymbol{K}}_{n+1}$ follow by linearization of the stress update (2) as

$$\hat{\boldsymbol{K}}_{n+1} \equiv \left(\partial \hat{\boldsymbol{P}} / \partial \boldsymbol{F}_{n+1}\right)\left(\boldsymbol{F}_{n+1};\ \text{state at } t_n,\ \Delta t\right). \tag{52}$$

Alternatively, the linearized virtual work principle (51) can be expressed in spatial form as

$$\int_{B_0} \nabla \boldsymbol{\eta} : \hat{\boldsymbol{k}}_{n+1} : \nabla \boldsymbol{u} \, \mathrm{d}V_0 - \text{forcing terms} = 0 \tag{53}$$

where ∇ is the spatial gradient operator and the spatial consistent tangents $\boldsymbol{k}$ are defined as

$$\hat{k}_{ijkl} = \hat{K}_{iJkL} F_{jJ} F_{lL}. \tag{54}$$

Whereas for small strains the computation of the consistent tangents reduces to a straightforward exercise for many commonly used models, for finite deformation formulations the calculations are considerably more cumbersome. It is, therefore, quite remarkable that in the case of single crystals the consistent tangents can be written down explicitly with some generality, as shown next.

6.2. State update

All the models discussed above, namely, the models of Pierce and co-workers (1983), section 2.2, Bassani and Wu (1989), section 2.3, and the dislocation model developed in the preceding sections, conform to the general constitutive framework summarized in box 2, which also shows the corresponding backward-Euler time discretization.

Box 2. State Update Algorithm

Constitutive:

$\mathbf{F} = \mathbf{F}^e\mathbf{F}^p;$

$\bar{\mathbf{C}}^e = \mathbf{F}^{eT}\mathbf{F}^e;$

$\dot{\mathbf{F}}^p\mathbf{F}^{p-1} = \sum_\alpha \dot{\gamma}^\alpha \bar{\mathbf{s}}^\alpha \otimes \bar{\mathbf{m}}^\alpha;$

$\bar{\mathbf{S}} = \bar{\mathbf{S}}(\bar{\mathbf{C}}^e);$

$\tau^\alpha = (\bar{\mathbf{C}}^e\bar{\mathbf{s}}^\alpha)^T\bar{\mathbf{S}}\bar{\mathbf{m}}^\alpha;$

$\dot{\gamma}^\alpha = \phi(\tau^\alpha, g^\alpha);$

$\dot{g}^\alpha = \sum_\beta h^{\alpha\beta}(\boldsymbol{\gamma})\dot{\gamma}^\beta;$

Incremental:

$\mathbf{F}_{n+1} = \mathbf{F}^e_{n+1}\mathbf{F}^p_{n+1}$

$\bar{\mathbf{C}}^e_{n+1} = \mathbf{F}^{eT}_{n+1}\mathbf{F}^e_{n+1}$

$(\mathbf{F}^p_{n+1} - \mathbf{F}^p_n)\mathbf{F}^{p-1}_{n+1} = \sum_\alpha \Delta\gamma^\alpha \bar{\mathbf{s}}^\alpha \otimes \bar{\mathbf{m}}^\alpha$

$\bar{\mathbf{S}}_{n+1} = \bar{\mathbf{S}}(\bar{\mathbf{C}}^e_{n+1})$

$\tau^\alpha_{n+1} = (\bar{\mathbf{C}}^e_{n+1}\bar{\mathbf{s}}^\alpha)^T\bar{\mathbf{S}}_{n+1}\bar{\mathbf{m}}^\alpha$

$\Delta\gamma^\alpha = \Delta t\phi(\tau^\alpha_{n+1}, g^\alpha_{n+1})$

$\Delta g^\alpha = \sum_\beta h^{\alpha\beta}(\boldsymbol{\gamma}_{n+1})\Delta\gamma^\beta$

For convenience, we have collected all slip strains in an array γ. Sums on α or β extend over the currently active slip systems, which for now we shall presume known. A procedure for determining the set of active slip systems is given in section 6.4.

The algorithm in box 2 defines a non-linear system of equations which can be solved for the updated state as a function of $\boldsymbol{F}_{n+1}$ and the initial conditions for the increment. A convenient method of solution consists of reducing the system to a set of equations for $\Delta\gamma$. This may be accomplished as follows. To avoid the numerical ill-conditioning which results from the frequently adopted power-law form of ϕ, we begin by inverting the discretized viscosity law and rewriting it as

$$\tau^\alpha_{n+1} = \psi(\Delta\gamma^\alpha/\Delta t, g^\alpha_{n+1}). \tag{55}$$

In this equation, g^α_{n+1} is a function of $\Delta\gamma$ through the hardening law. In addition, using the relations in box 2, τ^α_{n+1} can be written as a function of $\bar{\boldsymbol{C}}^e_{n+1}$ which, in turn, can be expressed in terms of $\Delta\gamma$ using the discretized flow rule. Thus, (55) defines a system of equations of the form

$$f^\alpha(\Delta\gamma) = \tau^\alpha_{n+1} - \psi(\Delta\gamma^\alpha/\Delta t, g^\alpha_{n+1}) = 0. \tag{56}$$

This system can now be solved by a Newton–Raphson iteration. A lengthy but straightforward computation yields the required Jacobian matrix $\partial f^\alpha/\partial(\Delta\gamma^\beta)$ explicitly. The resulting convergence rate is quadratic and convergence is typically achieved to within machine precision in two or three iterations.

6.3. Consistent tangents

The consistent tangents (54) for the update algorithm listed in box 2 can be computed in closed form. A trite calculation yields

$$\hat{k}_{ijkl} = k^{e}_{ijkl} - \sum_{\alpha}\sum_{\beta} A^{-1}_{\alpha\beta}(C^{e}_{ijmn}r^{\alpha}_{mn})(n^{\beta}_{pq}C^{e}_{pqkl}) - \sum_{\alpha}\sum_{\beta} A^{-1}_{\alpha\beta}(\tau_{in}r^{\alpha}_{jn} + \tau_{jn}r^{\alpha}_{in})(n^{\beta}_{pq}C^{e}_{pqkl}) \tag{57}$$

where

$$A^{\alpha\beta} = (1/\Delta t)\delta^{\alpha\beta} + n^{\alpha}_{ij}C^{e}_{ijkl}r^{\beta}_{kl} - (\partial\phi^{\alpha}/\partial g^{\alpha})\tilde{h}^{\alpha\beta} \tag{58}$$

$$\tilde{h}^{\alpha\beta} = h^{\alpha\beta} + \sum_{\gamma}\frac{\partial h^{\alpha\gamma}}{\partial\gamma^{\beta}}\Delta\gamma_{\gamma} \tag{59}$$

$$n^{\alpha}_{ij} = (\partial\phi^{\alpha}/\partial\bar{S}_{IJ})F^{e-1}_{Ii}F^{e-1}_{Jj} \tag{60}$$

$$r^{\alpha}_{ij} = \bar{R}^{\alpha}_{IJ}F^{e-1}_{Ii}F^{e-1}_{Jj} \tag{61}$$

$$\bar{R}^{\alpha}_{IJ} = \bar{C}^{e}_{IK}\bar{s}^{\alpha}_{K}\bar{m}^{\alpha}_{L}(F^{p}_{n})_{LA}F^{p-1}_{AJ} \tag{62}$$

$$C^{e}_{ijkl} = (\partial\bar{S}_{IJ}/\partial\bar{C}^{e}_{KL})F^{e-1}_{Ii}F^{e-1}_{Jj}F^{e-1}_{Kk}F^{e-1}_{Ll} \tag{63}$$

and we have dropped the subindex $n+1$ from all updated quantities. In these definitions C^{e}_{ijkl} are the spatial elastic moduli and $\boldsymbol{n}^{\alpha}$ and $\boldsymbol{r}^{\alpha}$ play the role of effective spatial normal and plastic flow direction, respectively. As expected from general results on finite plasticity (see, e.g. Moran *et al* 1990), the consistent tangents (57) are generally unsymmetric.

The use of a set of exact tangents ensures a quadratic asymptotic rate of convergence of the global equilibrium iterations. In order to increase the radius of convergence of the Newton–Raphson iteration, it is often convenient to perform line searches to scale the incremental displacements. Practical line search methods are reviewed by Crisfield (1991).

6.4. Determination of the active slip systems

In the foregoing discussion the set of active slip systems has been presumed known. In a typical calculation, the pattern of slip activity changes with deformation and the active set has to be continuously updated. We define the active set $\mathcal{L}$ as the set of systems α such that $\tau^{\alpha}_{n+1} > g^{\alpha}_{n+1}$. The flowchart of an iterative algorithm for determining the active set is given in box 3.

Box 3. Determination of Active Systems

i) Initialize $\mathcal{L} = \emptyset$.
ii) Compute $\Delta\gamma^{\alpha}$ based on current $\mathcal{L}$.
iii) If $\Delta\gamma^{\alpha} < 0$ remove α from $\mathcal{L}$, set $\Delta\gamma^{\alpha} = 0$.
iv) Update remaining state variables based on current $\Delta\gamma^{\alpha}$.
v) Is $\tau^{\alpha}_{n+1} \leq g^{\alpha}_{n+1}$ $\forall\alpha$ not in $\mathcal{L}$?.
NO: Add most loaded system(s) α (i. e., maximum $\tau^{\alpha}_{n+1} - g^{\alpha}_{n+1}$) to $\mathcal{L}$;
GO TO (ii).
YES: EXIT.

Evidently, the starting iteration of the algorithm corresponds to an elastic update. For single-yield surface models, the search stops after at most an additional iteration, and the

algorithm reduces to the conventional elastic-predictor/plastic-corrector implementation of implicit updates. If a largely stable set of active systems is anticipated for a given loading path, it may prove advantageous to replace the default initialization, $\mathcal{L} = \emptyset$, to the set of active systems from the previous converged solution, whereupon the searching algorithm converges in one iteration for as long as the slip pattern remains unchanged.

6.5. *Adaptive meshing*

Plastic regions in crystals are often narrow and elongated, and extend along well defined crystallographic directions. The slip patterns induced by cracks in single crystals are a case in point, as demonstrated by the numerical simulations presented in section 8. Under these conditions, the velocity field and other aspects of the solution exhibit a rapid variation across the plastic zones while varying slowly in other directions. In cases where the geometry of the evolving fields is not known *a priori*, adaptive meshing techniques furnish an effective device for resolving the fine structure of the solution.

For the applications discussed in section 8, an adaptation criterion based on the equidistribution of plastic work has proven useful. In this approach, elements with a plastic work contents exceeding a prescribed tolerance TOL, i.e. elements such that

$$\int_{\Omega_h^e} W^p \, d\Omega > \text{TOL} \tag{64}$$

are targeted for refinement. Here, Ω_h^e denotes the domain of element e and, for crystals, the plastic work density W^p is given by

$$W^p = \int_0^t \left(\sum_\alpha \tau^\alpha \dot{\gamma}^\alpha \right) dt. \tag{65}$$

Clearly, this criterion leads to refinement in regions of high plastic deformation. In simulations involving cracks subjected to monotonically increasing loads (cf section 8), the plastic work equidistribution criterion results in continuous generation of elements at the tip and enables the mesh to track the expanding plastic regions.

A remeshing technique for finitely deforming plastic solids has been proposed by Ortiz and Quigley (1991). In this approach, meshes consisting of six-noded triangular elements with three quadrature points and constant pressure are constructed by Delaunay triangulation (Sloan 1987). The connectivity of the mesh is determined from the set of corner nodes of the elements, with the midnodes added subsequently. The mesh is adapted at regular intervals by adding new corner nodes at the midsides of elements targeted for refinement. The element connectivity is then completely redefined by a Delaunay triangulation based on the new set of corner nodes. In particular, no hierarchical compatibility between subsequent meshes is enforced. After each triangulation, Crane and co-workers' (1976) implementation of Gibbs and co-workers' (1976) bandwidth minimization algorithm is applied. Finally, a variationally consistent transfer operator proposed by Ortiz and Quigley (1991) is used to transfer the state variables between meshes following an adaptation.

The plastic work equidistribution criterion is amenable to an error minimization interpretation in some simple cases. To illustrate this connection, consider the case of a solid deforming in antiplane shear relative to the $x_1 - x_2$ plane. Let the solid obey J_2-deformation theory of plasticity with power-law hardening. The equation governing the out-of-plane displacement $u(x_1, x_2)$ is

$$\begin{aligned} &\nabla \cdot (|\nabla u|^{\beta-2} \nabla u) = f && \text{in } \Omega \\ &u = 0 && \text{on } \partial\Omega \end{aligned} \tag{66}$$

where n is the hardening exponent, $\beta = (n+1)/n$ and, for simplicity, we assume homogeneous Dirichlet boundary conditions. Under suitable restrictions on the forcing f, an appropriate solution space for u is the Sobolev space $W_0^{1,\beta}(\Omega)$ (see, e.g. Oden *et al* 1986). Under these conditions, the plastic work in element e is given by the energy seminorm, i.e.

$$\int_{\Omega_h^e} W^p \, d\Omega = \frac{1}{\beta} |u_h^e|^{\beta}_{W_0^{1,\beta}(\Omega_h^e)} \tag{67}$$

where u_h^e is the finite-element solution over element Ω_h^e. Therefore, in this case equidistributing plastic work is equivalent to equidistributing the energy over the mesh.

This affords an illuminating connection between plastic work equidistribution and the interpolation error method of Diaz and co-workers (1983). Let $\tilde{u}_h^e$ be the interpolant over Ω_h^e derived from the nodal values of u. Let $k \geqslant 0$ and $m \geqslant 0$ be integers and $p, q \in [1, \infty]$ be numbers such that $W^{k+1,p}(\Omega_h^e)$ is contained in $W^{m,q}(\Omega_h^e)$ with a continuous injection. Let the interpolation functions in Ω_h^e include the complete set of polynomials up to order k. Then (Ciarlet 1978), there exists a constant C such that, for all $u^e \in W^{k+1,p}(\Omega_h^e)$,

$$E_h^e \equiv |u^e - \tilde{u}_h^e|_{m,q,\Omega_h^e} \leqslant C[\text{meas}(\Omega_h^e)]^{1/q-1/p}\left[(h^e)^{k+1}/(\rho^e)^m\right]|u^e|_{k+1,p,\Omega_h^e} \tag{68}$$

where u^e is the restriction of u to Ω_h^e, $\text{meas}(\Omega_h^e)$ is the measure of Ω_h^e and ρ^e the diameter of the largest ball contained in Ω_h^e. The requisite continuous injection condition is satisfied if (Ciarlet 1978)

$$1/q = 1/p - (k+1-m)/d \qquad k+1-m < d/p \tag{69}$$

where d is the number of spatial dimensions. These requirements are satisfied by, for instance, taking $q = p = 2$ and $k+1 = m$, which is the case considered by Diaz and co-workers (1983). In (68), E_h^e may be regarded as a measure of the local interpolation error over Ω_h^e. The sum $E_h = \sum_e E_h^e$ measures the ability of the mesh to *resolve* the solution u. If the finite-element approximation interpolates well the exact solution, $|u^e|_{k+1,p,\Omega_h^e}$ in (68) can be replaced by the norm $|u_h^e|_{k+1,p,\Omega_h^e}$ of the computed solution u_h^e. Then, a minor extension of a proof by Devloo and co-workers (1987) shows that the mesh which minimizes E_h for a fixed number of elements NUMEL is that for which $(h^e)^{\alpha}|u_h^e|_{k+1,p,\Omega_h^e}$, $\alpha = k+1-m$, takes a uniform value on all elements. If, for instance, the interpolation error is measured in terms of the energy norm, which corresponds to setting $q = p = \beta$ and $k = 0$, $m = 1$, then $\alpha = 0$ and the optimality condition amounts to equidistributing the energy norm. Therefore, for the model problem under consideration, equidistribution of plastic work does indeed lead to the minimization of the interpolation error as measured by the energy norm.

7. Comparison with experiment

Latent hardening (Kocks 1964, Ramaswami *et al* 1965, Kocks and Brown 1966, Franciosi *et al* 1980, Bassani and Wu 1989) and multislip tests (Kocks 1960, Ambrosi *et al* 1974, Schwink and Göttler 1976, Miura *et al* 1977, Franciosi and Zaoui 1982) have been widely used to investigate the hardening behavior of single crystals. In latent-hardening experiments, the crystal is first oriented for single slip and loaded in uniaxial tension or compression. The crystal is subsequently cut into smaller specimens which are rotated

and re-loaded so as to activate secondary systems. This type of test enables a direct characterization of the hardening induced in secondary systems by plastic activity in the primary slip system, or latent hardening. In multislip tests, the crystal is loaded uniaxially in a direction of high symmetry, with the result that several slip systems are simultaneously activated. It is often the case that, from a purely kinematic standpoint, the imposed deformation can be accommodated by more than one combination of active slip systems. However, the choice of slip pattern can have a marked influence on the resulting stress–strain curve. Multislip experiments are especially useful for elucidating these issues.

Table 1. Material constants.

Elastic Constant C_{11}	168.4×10^3 MPa
Elastic Constant C_{12}	121.4×10^3 MPa
Elastic Constant C_{44}	75.4×10^3 MPa
g_0	2.0 MPa
$\dot{\gamma}_0$	$1\ s^{-1}$
m	0.01
α	0.3
b	2.56×10^{-10} m
γ_{sat}	0.5%
ρ_0	$10^{12}\ m^{-2}$
ρ_{sat}	$10^{15}\ m^{-2}$
a_0	75×10^{-5}
a_1/a_0	5.7
a_2/a_0	10.2
a_3/a_0	16.6

In this section we present comparisons between both multislip and latent-hardening experiments and the dislocation theory developed in the foregoing. Here we shall restrict our attention to copper single crystals. The theoretical curves are obtained by numerical integration of the dislocation model using the backward-Euler algorithm of box 2. All curves are reported in terms of nominal stress and engineering strain. A system α is considered to be active when $\tau^\alpha > g^\alpha$, i.e. when the resolved shear stress on the system exceeds its yield stress. The simulations reported here are performed using a single eight-node brick finite element. The tensile direction is aligned with the element axes. The two loaded faces of the cube are constrained to remain parallel to each other and perpendicular to the loading axis. These boundary conditions simulate a stiff loading device in which the clamps are prevented from rotating. The values of the material constants employed in the calculations are listed in table 1.

7.1. Multislip tests

Figure 5 shows a comparison between theoretical and experimentally determined uniaxial tension stress–strain curves for copper single crystals. The experimental data is taken from Franciosi and Zaoui (1982). With the notable exception of the [001]–[111] zone axis, the experimental record shows that the majority of high symmetry tensile directions result in substantial amounts of single slip prior to the inception of multiple glide. Even for the [001]–[111] zone axis, however, the relative extents of plastic activity in the various slip systems vary in time, with different combinations of systems dominating the early and late stages of deformation depending on the orientation of the tensile axis.

Our numerical simulations are indicative of a very high sensitivity of the behavior of the crystal to small misalignments of the loading axis. Small deviations of the axis ($< 1°$) from

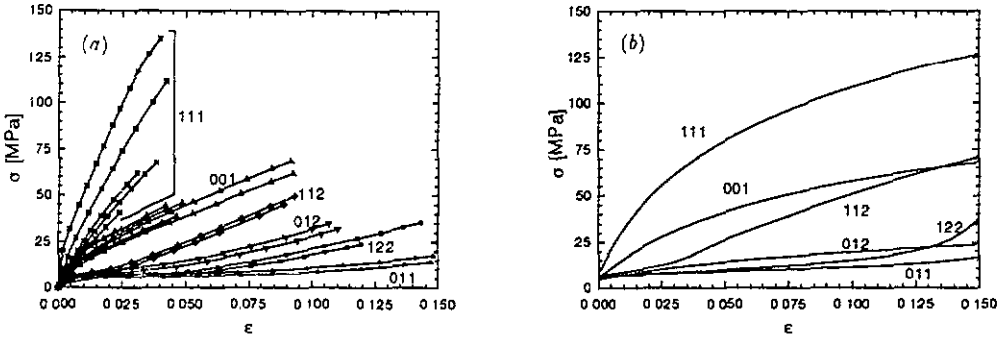

Figure 5. Uniaxial tension test for copper single crystals: (*a*) experimental measurements (Franciosi and Zaoui 1982); (*b*) dislocation model.

its nominal direction give rise to variations in the pattern of slip activity and to substantial quantitative differences in the predicted stress–strain curves. This high sensitivity may partly account for the considerable scatter in experimental stress–strain curves obtained under nominally identical conditions (figure 5). The sensitivity to misalignments of the loading axis is particularly acute for high-symmetry orientations of the crystal.

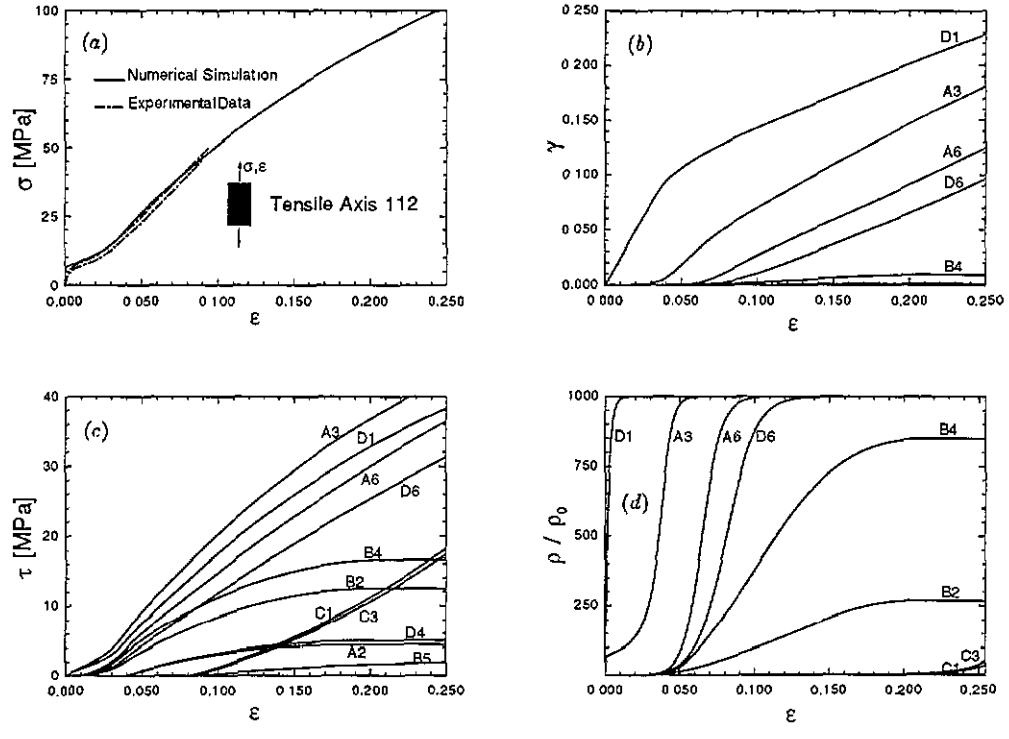

Figure 6. Tensile axis [112]: (*a*) stress–strain curve; (*b*) slip strains; (*c*) resolved shear stresses, and (*d*) dislocation densities.

Figure 6(*a*) compares theoretical versus experimental (Franciosi and Zaoui 1982) stress–

strain curves for a crystal loaded in uniaxial tension in the [112] direction. A good overall agreement between the two sets of curves is evident from the figure. Due to a small misalignment in the loading axis intentionally introduced in the simulations, system D1 yields first. (Here and subsequently, we adhere to the standard Schimd and Boas convention for designating the slip systems of an FCC crystal.) During the early stages of deformation, easy glide by single slip on system D1 is predicted. At about 3% deformation, the additional system A3 is activated, and an attendant upturn in the stress–strain curve is observed. An upturn of this type is commonly identified with the inception of stage II of hardening. The variation of the relevant slip strains with deformation is shown in figure 6(*b*). The ranges of deformation where single and multiple slip are dominant are clearly identifiable in the figure.

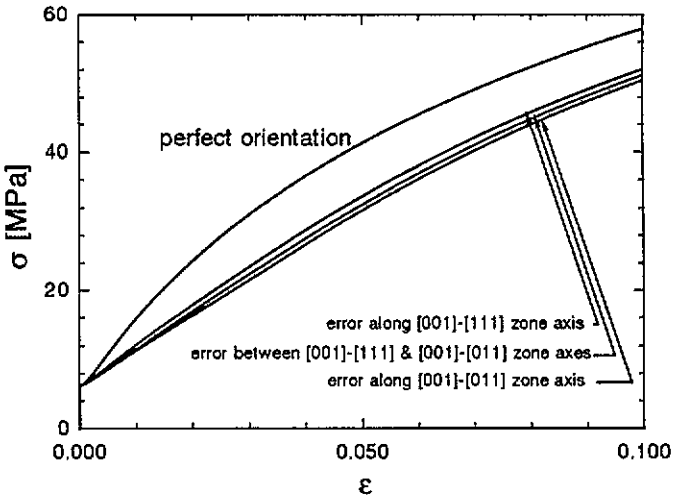

Figure 7. Theoretical stress–strain curves for various misalignments of the [001] tensile axis.

The precise manner in which small misalignments of the loading axis produce large variations in the response bears some emphasis. For uniaxial loading in the [112] direction, the resolved shear stresses on systems A3 and D1 are identical under nominal conditions. However, in our numerical simulation the axis misorientation causes yielding in system D1 to occur slightly in advance of its nominal inception point (figure 6(*b*)). The exponential dislocation multiplication law (49) then produces a precipitous increase in the obstacle density on all other systems (figure 6(*d*)), with an attendant rapid rate of hardening as measured by τ_c, equation (41). Eventually, the resolved shear stress on A3 reaches the yield level, which has hitherto remained near its initial value. With the ensuing slip, A3 hardens and its resolved shear stress remains close to that of D1 (figure 6(*c*)). Interestingly, although some plastic activity on A3 is recorded during stage I ($\epsilon < 3\%$), the resulting slip strains are negligible in this range when compared to those on D1. In this sense, D1 is overwhelmingly dominant and the crystal may be regarded as undergoing single slip. When the saturation slip strain $\gamma_{sat} = 0.5\%$ is attained (figure 6(*b*)) the rate of dislocation multiplication on D1, and the rate of hardening on all other systems, slow down considerably. This allows A3, and other systems subsequently, to become active, thus bringing the single-slip regime to an end.

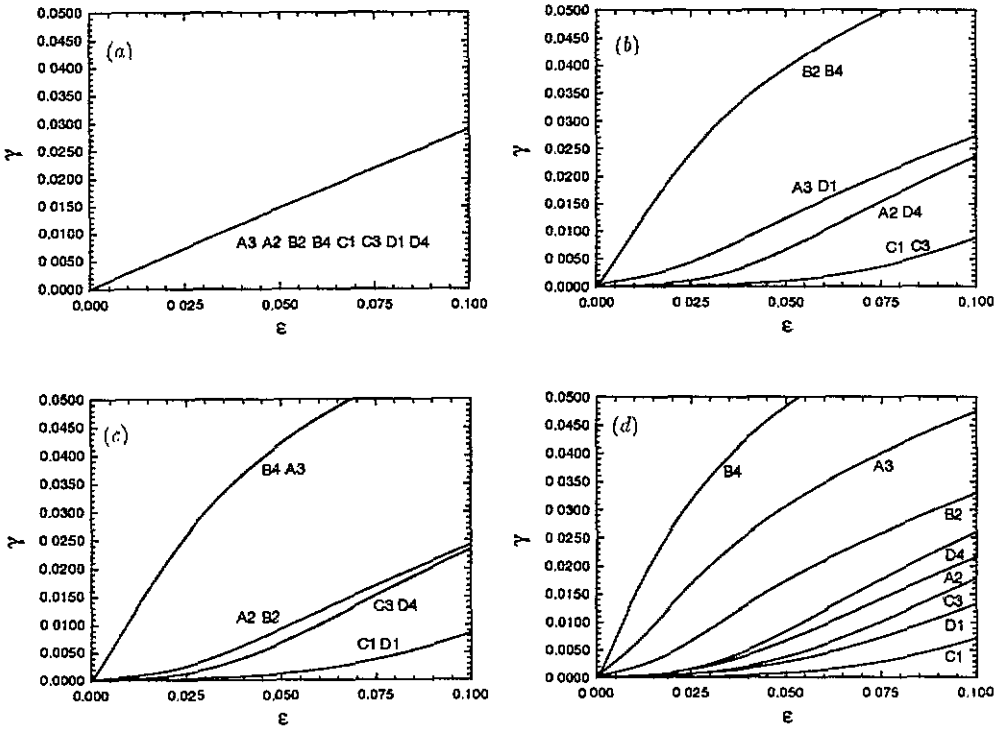

Figure 8. Slip strains, [001] tensile axis: (*a*) perfect alignment of the loading axis; (*b*) misalignment along the [001]–[111] zone axis; (*c*) misalignment between the [001]–[111] and [001]–[011] zone axes; and (*d*) misalignment along the [001]–[011] zone axis.

In summary, two main mechanisms are responsible for the single–multiple slip transition. The first factor is geometrical in nature, and concerns the small variations in resolved shear stress between nominally identical systems introduced by slight misalignments of the loading axis. Indeed, simulations based on a mathematically exact orientation of the crystal predict simultaneous slip on all nominally active systems and fail to exhibit a stage I–stage II transition. By itself, a misorientation of the loading axis would not be sufficient to cause large variations in the behavior of the crystal were it not for the exponential growth capable of being sustained by the dislocation densities prior to saturation. The rapid pace of dislocation multiplication in the system which yields earliest causes the remaining nominally active systems to harden, thus delaying their activity.

The misorientation sensitivity in the response of the crystal is exacerbated in situations where the loading axis coincides with a direction of high symmetry. To illustrate this effect, we next consider the configuration of highest possible symmetry, namely, a [001] tensile axis. For this orientation, eight slip systems are potentially active. We have considered four orientations of the tensile axis differing by less than 0.5 °: (*a*) a mathematically exact [001] tensile axis; (*b*) a misalignment along the [001]–[111] zone axis; (*c*) a misalignment between the [001]–[111] and [001]–[011] zone axes; and (*d*) a misalignment along the [001]–[011] zone axis. Figure 7 compares the predicted stress–strain curves. A wide spread in the results is clearly apparent, with the stiffest response occurring for the perfectly aligned axis. During the early stages of deformation, the rate of hardening is also highest in the

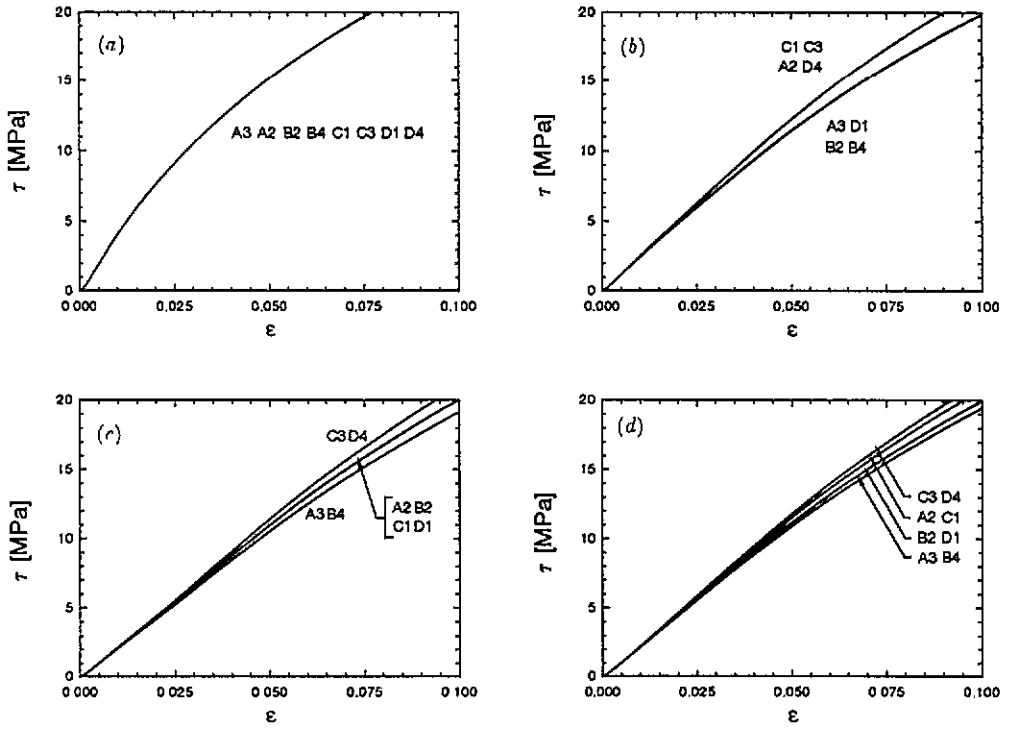

Figure 9. Resolved shear stresses, [001] tensile axis: (*a*) perfect alignment of the loading axis; (*b*) misalignment along the [001]–[111] zone axis; (*c*) misalignment between the [001]–[111] and [001]–[011] zone axes; and (*d*) misalignment along the [001]–[011] zone axis.

perfectly oriented crystal. Subsequently, the hardening rates become ostensibly identical in all cases.

The discrepancies in the patterns of slip activity are even more pronounced (figure 8). Under nominal conditions, all eight potentially active systems yield simultaneously (figure 8(*a*)). For the misoriented crystals, the activity of some systems is significantly delayed (figure 8(*b*)–(*d*)). In all cases, the slip activity is consistent with the symmetries preserved by the misalignment of the axis. By way of example, in case (*b*) the pairs of systems B2–B4, A3–D1, A2–D4 and C1–C3 slip by the same amount. As expected, all eight systems exhibit different slip activities in case (*d*), in which no symmetries are preserved.

The causes underlying the observed variations in the response of the crystal with misorientation are similar to those noted in the case of loading in the [112] direction. As is evident from figure 8, the slip activity in the most loaded systems has the effect of inhibiting slip in the remaining systems up until saturation. Remarkably, despite the wide disparity in slip activities the resolved shear stress and hardening rate remain nearly the same in all systems (figure 9), as required by equilibrium. It is interesting to note that, owing to the high symmetry of the loading axis, the lattice rotations remain small at all times. The lag introduced by misorientation in the activity of certain systems is also evident in figure 10, which shows the evolution of dislocation densities. The most loaded systems exhibit rapid growth initially and then quickly saturate. At this point, their inhibiting effect on the remaining systems stops. The increased activity in these systems accounts for the

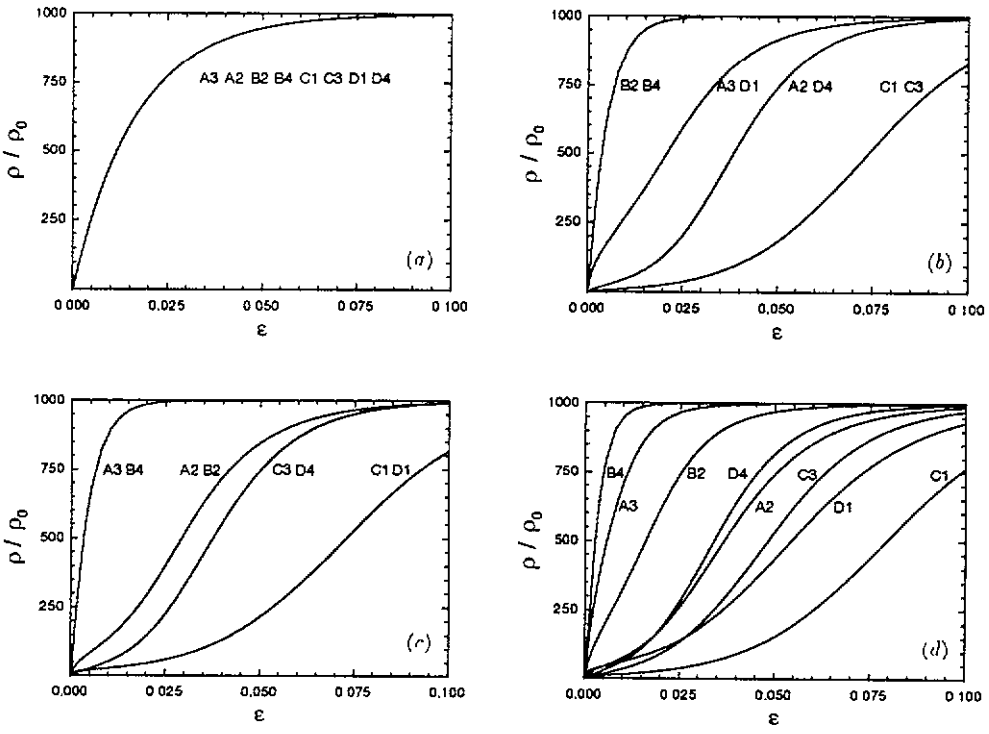

Figure 10. Dislocation densities, [001] tensile axis: (*a*) perfect alignment of the loading axis; (*b*) misalignment along the [001]–[111] zone axis; (*c*) misalignment between the [001]–[111] and [001]–[011] zone axes; and (*d*) misalignment along the [001]–[011] zone axis.

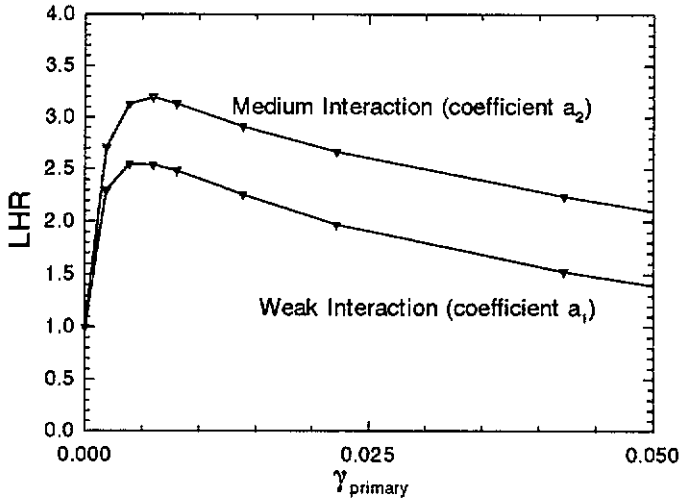

Figure 11. Computed latent hardening ratios (LHR) as a function of primary shear strain for different interaction coefficients a_i.

sudden upturn in their rate of dislocation multiplication (figure 10).

7.2. Latent-hardening tests

In latent-hardening tests, secondary flow stresses are determined from the reloading stress–strain curve by back-extrapolation. A shortcoming of this procedure is that, because the reloading curves need not tend to a straight asymptote, the measurements are sensitive to the offset shear strain chosen. Therefore, comparisons between theory and experiment must necessarily be qualitative in nature.

Latent-hardening data are often reported in terms of the latent-hardening ratio LHR = τ_s/τ_p, where τ_p and τ_s denote the flow stresses of the primary and secondary slip system, respectively. Figure 11 shows theoretical plots of the LHR as a function of the prestrain γ_p on the primary system and the strength of the interaction between the primary and secondary systems, as measured by the coefficients a_i (section 4). In keeping with the experimental procedure, the computed values of the flow stresses are obtained from the reloading stress–strain curve by backextrapolation to $\gamma_s = 0$. Theory and experiment are in good qualitative agreement as regards the dependence of the LHR on prestrain. The initial value of LHR = 1 is a direct consequence of its definition and of the fact that, for an FCC crystal, the initial flow stress in a well annealed crystal is the same in all systems. The LHR subsequently goes through a maximum and then settles down to a value which remains nearly constant under increasing prestrain.

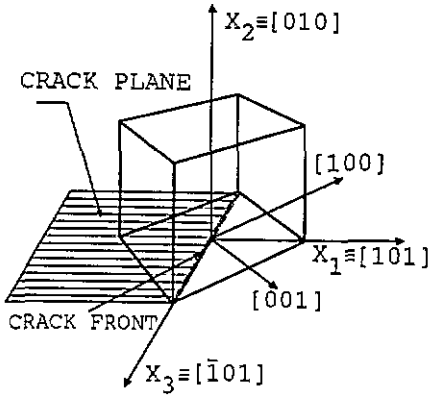

Figure 12. Crack on (010) plane in an FCC crystal with the crack front parallel to $[\bar{1}01]$.

The mechanisms underlying this dependence bear some interest. In the prestraining stage, the variation of τ_s is determined by dislocation multiplication on the primary system and the attendant increase in the density of point defects on the secondary system. By contrast, the variation of τ_p in the same stage solely reflects the self-hardening of the primary system. Because of the exponential growth in dislocation density on the primary system, for small prestrains τ_s attains values considerably in excess of τ_p, and hence the initial precipitous increase in the LHR with prestrain (figure 11). For prestrains such that $\gamma_p \gg \gamma_{sat}$, the dislocation density on the primary system saturates and τ_s attains a nearly constant value. At the same time, τ_p continues to grow slowly due to self-hardening of the primary system, and a downturn in the LHR-γ_p curve ensues (figure 11).

As a general rule, the stronger the interaction between primary and secondary slip systems (i.e. the larger the interaction coefficient a_i), the higher the resulting value of the LHR (figure 11). However, for very strong interactions, such as those described by a_3,

the pattern of slip activity may deviate from that expected in latent-hardening experiments, and caution must be exercised in interpreting the results. Thus, for strongly interacting systems τ_s rises sharply over τ_p even for small prestrains. Upon reloading, τ_s may be so large that the primary system remains dominant. This situation tends to perpetuate itself, since the absence of any significant slip on the secondary system keeps the primary system comparatively soft and, in addition, the continuing activity of the primary system contributes to harden the secondary system further. By contrast, in cases where the primary and secondary systems interact weakly (e.g. coefficients a_1 and a_2), the secondary system slips at a rate sufficient to keep the primary system from become active during the reloading stage, as befits latent-hardening experiments. These predicted differences in behavior for varying interaction strengths are in full agreement with the observations of Franciosi and Zaoui (1982).

8. Numerical simulation of cracks in single crystals

Calculations of near-tip fields in single crystals provide an example of application of the methodology described in previous sections. The specific boundary value problem analyzed is that of a crack on the (010) plane of a copper single crystal, with the crack front in the $[\bar{1}01]$ direction, and crack growth along [101] (figure 12). Combinations of slip systems which result in plane-strain deformations are pairs of the type (111) $[1\bar{1}0]$ and (111) $[0\bar{1}1]$, which jointly give rise to effective in-plane shear along the $[1\bar{2}1]$ direction (figure 13). Similarly, the systems $(1\bar{1}1)$ [110] and $(1\bar{1}1)$ [011] combine to produce effective in-plane slip along the [121] direction. Finally, the pair of systems $(11\bar{1})$ [101] and $(\bar{1}11)$ [101] operating jointly also result in plane-strain deformations. The small-strain yield surface corresponding to this case is shown in figure 14.

The finite-deformation case has proven intractable by analytical means and has to be dealt with numerically. Figure 15 shows the initial finite-element mesh used in the computations. We have chosen to round the tip of the crack into a circular notch or root radius r_0 (figure 15(a)). The initial mesh is fan-like, and divides the upper half-plane into eight equal sectors centered at the tip (figure 15(b)). The ratio of the radius R of the remote boundary to the notch root radius is 10^4. The crack opening is driven by prescribing the anisotropic elastic K-field displacements on the remote boundary. The crack is loaded up to a maximum value of $K/(g_0\sqrt{R}) = 5$.

At this point, the root radius of the notch has expanded by 20%, and the maximum slip strains are of the order of 10^3 times the initial yield strain. Intentionally, the initial mesh is too coarse to adequately resolve the solution. To provide the requisite resolution, we resort to the adaptive meshing technique described in section 6.5. The final mesh is shown in figure 16. The value of the plastic work contents at which an element is targeted for refinement is $\text{TOL}/(r_0^2 g_0^2/C_{44}) = 1.5 \times 10^{-7}$. The calculations are based on the dislocation model described in section 5. The material constants adopted in the analysis are listed in table 1.

The following terminology proves helpful in interpreting the results of the calculations. For cracks loaded in mode I, plastic shearing on the most active slip systems can occur either parallel or perpendicular to the active slip planes. Shearing parallel to slip planes, or *shear* mode, is accommodated by edge dislocations emanating from the crack tip. Thus, in the shear mode, the crack tip itself acts as dislocation source. By way of contrast, shearing perpendicular to the slip planes, or *kink* mode, necessitates the formation of dislocation dipoles (Cahn 1951). The activation of this mode requires abundant internal sources of

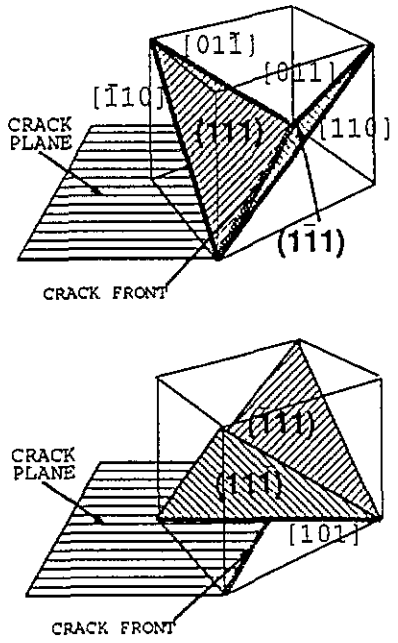

Figure 13. Slip systems capable of producing sustained plane-strain plastic deformations.

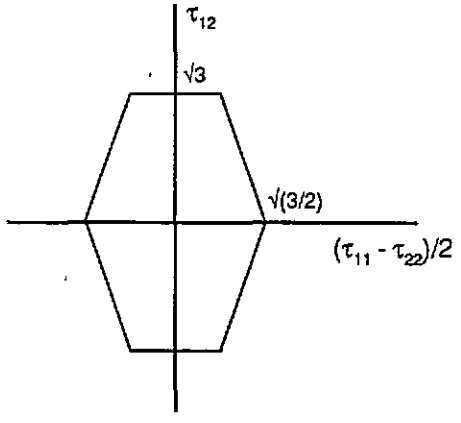

Figure 14. Small-strain yield surface for an FCC crystal with the orientation shown in figure 12 undergoing plane-strain deformation.

dislocation emission. Kink modes of deformation involve extensive lattice rotations, which may in turn induce geometric hardening or softening depending on the direction of rotation (Asaro 1983).

Figure 17 (see page 258) shows the computed isocontours of slip activity in the small-strain region away from the crack tip. The dominant slip modes are three: (i) a shear mode on (1$\bar{1}$1) [011] and (1$\bar{1}$1) [110] at 55°; (ii) a kink mode on (11$\bar{1}$) [101] and ($\bar{1}$11) [101]

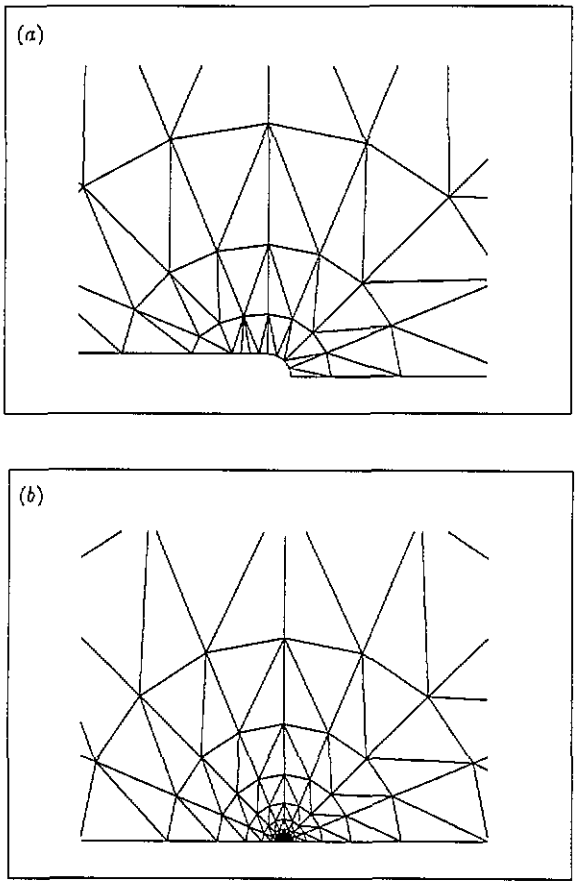

Figure 15. Initial mesh containing 256 six-node triangular elements: (*a*) close-up view of the near-tip region; (*b*) overall view of the mesh.

at 90°; and (iii) a shear mode at 145 ° on (111) $[1\bar{1}0]$ and (111) $[0\bar{1}1]$. The variation of the components of the Kirchhoff stress tensor and the slip strains with the polar angle θ is shown in figure 18(*a*) and (*b*), respectively. It is clear from these figures that the three dominant slip modes determine directions of rapid variation of displacements and stresses. The adaptive meshing procedure effectively provides adequate mesh resolution in those regions.

Figure 19 shows the isocontours of slip activity at closer range to the crack tip. The slip pattern changes as a result of the emergence of two additional kink modes: one on system (111) $[\bar{1}2\bar{1}]$ at 40°; and a second mode on $(1\bar{1}1)$ [121] at 170°. As is evident from figure 20(*a*) and (*b*) the slip strains and stresses vary slowly with θ in this region. Consequently, the adaptation procedure gives rise to a less structured mesh.

9. Discussion

Cracks in single crystals have been investigated by Rice and Nikolic (1985) and Rice (1987) within the framework of small-strain ideal plasticity, and by Rice and Saeedvafa (1988) and

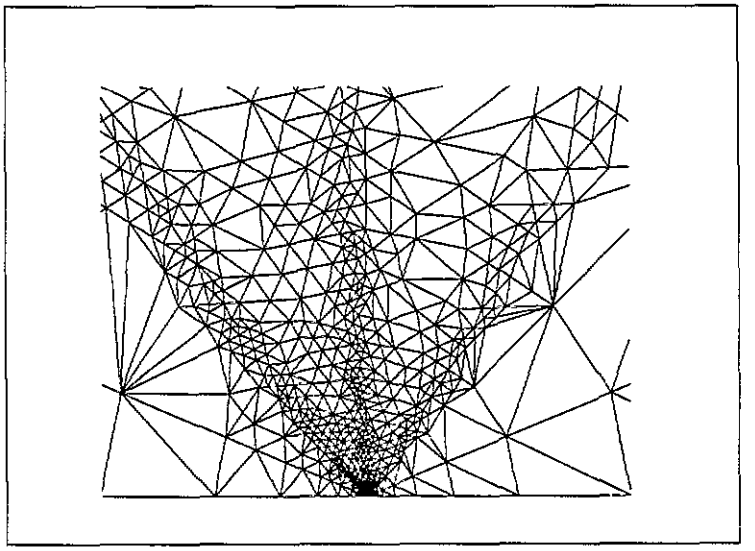

Figure 16. Final mesh containing 2700 elements.

Saeedvafa and Rice (1989), who also restricted their analysis to small strains and no lattice rotations but allowed for Taylor, or isotropic, power-law hardening. Mohan and co-workers (1992a,b) subsequently analyzed cracks of the same geometry by means of a geometrically rigorous formulation which accounted for finite lattice rotations. The calculations were based on the formulation of Pierce and co-workers (1983), and on a phenomenological hardening law proposed by Chang and Asaro (1981) for Al–Cu alloys (cf section 2.3). The crystals described by this law exhibit a first stage of rapid hardening followed by ideally plastic behavior. This is in sharp contrast to the stage I–stage II structure of the hardening of single-phase FCC crystals. For some orientations, the results of Mohan and co-workers (1992a,b) differ from the predictions of the small-strain theory, but are in good overall agreement with the experimental observations of Shield and Kim (1990). These analyses, together with the simulations described in section 8, illustrate the strong influence of the kinematic assumptions and the details of the hardening law on solutions to specific boundary value problems.

Rice (1987) gave an analytical solution to the problem considered in section 8 under the assumption of small strains and lattice rotations and ideal rigid-plastic behavior. Rice additionally assumed that the solid was at yield everywhere, so that the stresses were constrained to lie on a fixed hexagonal yield surface in the $(\sigma_{11}-\sigma_{22})/2-\sigma_{12}$ stress plane (figure 14). Under these conditions, Rice (1987) obtained an analytical solution by piecing together four sectors of constant stress and double slip. These sectors were separated by three radial lines of displacement and stress discontinuity representing narrow regions of single slip. The rays of discontinuity at 54.7° and 125.3° support shear modes on $(2\bar{1}\bar{1})$ [111] and (211) $[1\bar{1}\bar{1}]$, while the discontinuity at 90° to the plane of crack corresponds to a kink mode on (011) $[1\bar{1}1]$ and (011) $[11\bar{1}]$. Figure 21(a) shows the trajectory obtained in the stress plane by sampling the solution on a semicircle centered at the tip, with θ varying between the limits 0 and π, corresponding to the half-plane following the crack and the upper crack face, respectively. The stress θ trajectory effects a half turn around the yield surface.

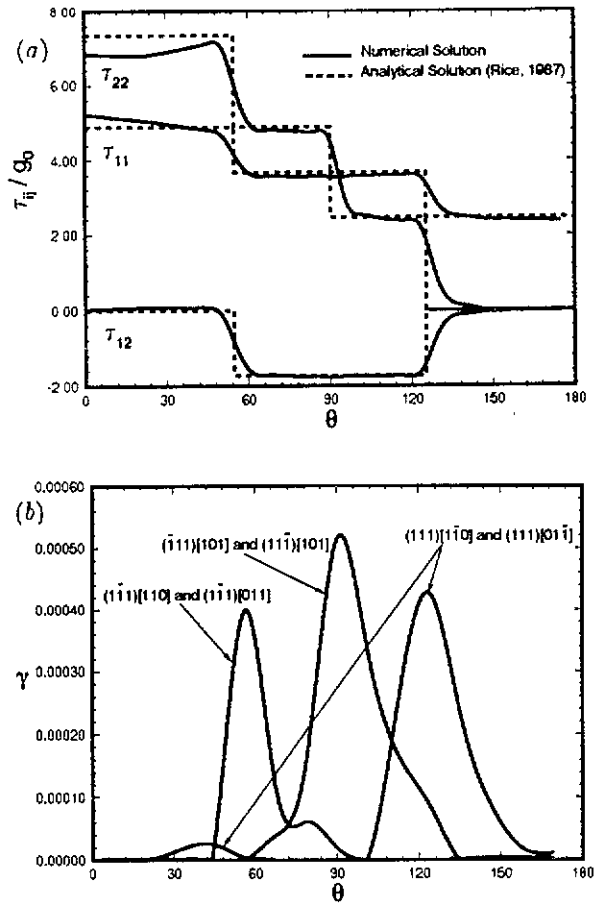

Figure 18. Variation of (*a*) the components of the Kirchhoff stress tensor and (*b*) the slip strains as a function of the polar angle at $r = 0.18R$.

Evidently, the numerical solution given in section 8 agrees closely with Rice's (1987) solution in the outer section of the plastic zone (figure 18). This owes to the fact that, in that region, strains and lattice rotations are small and the crystal deforms by easy glide, which can be idealized as perfectly plastic behavior to a good approximation. These are precisely the conditions under which Rice's (1987) solution applies. Closer to the tip, the crystal enters stage II of hardening. This stage is characterized by strong interactions between the slip systems and by rapid hardening. The computed slip strain variation with polar angle θ is depicted in figure 20. A noteworthy feature of the slip pattern is the presence of *triple-glide* sectors. This is in contrast with the structure of the solution in the easy glide region, which consists of sectors of single and double glide only. This limitation is peculiar to Taylor or isotropic hardening models such as those considered by Rice (1987) and Saeedvafa and Rice (1989), for which the yield surface is constrained to remain undistorted. Figure 21(*b*) shows the computed θ trajectory in Kirchhoff stress space normalized by the resolved shear stress τ_M in the most active slip system. The stress trajectory nearly effects a full turn

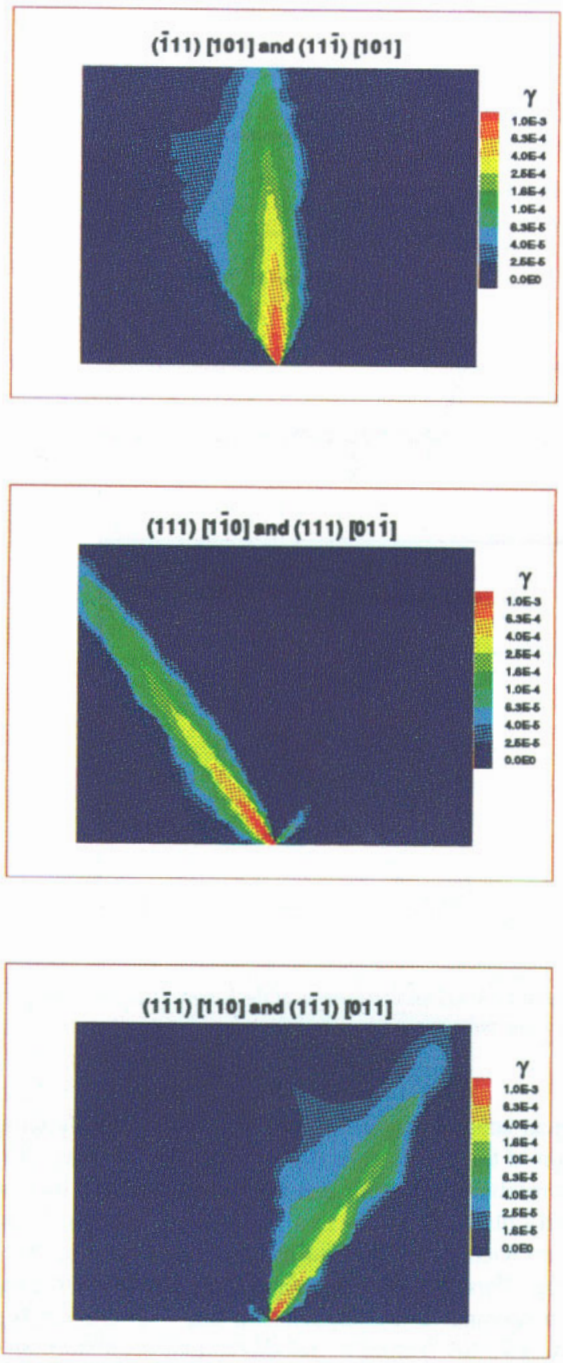

Figure 17. Isocontours of slip strain in the small-strain region away from the crack tip.

around the origin. It bears emphasis that the calculations predict all of the solid to be at yield.

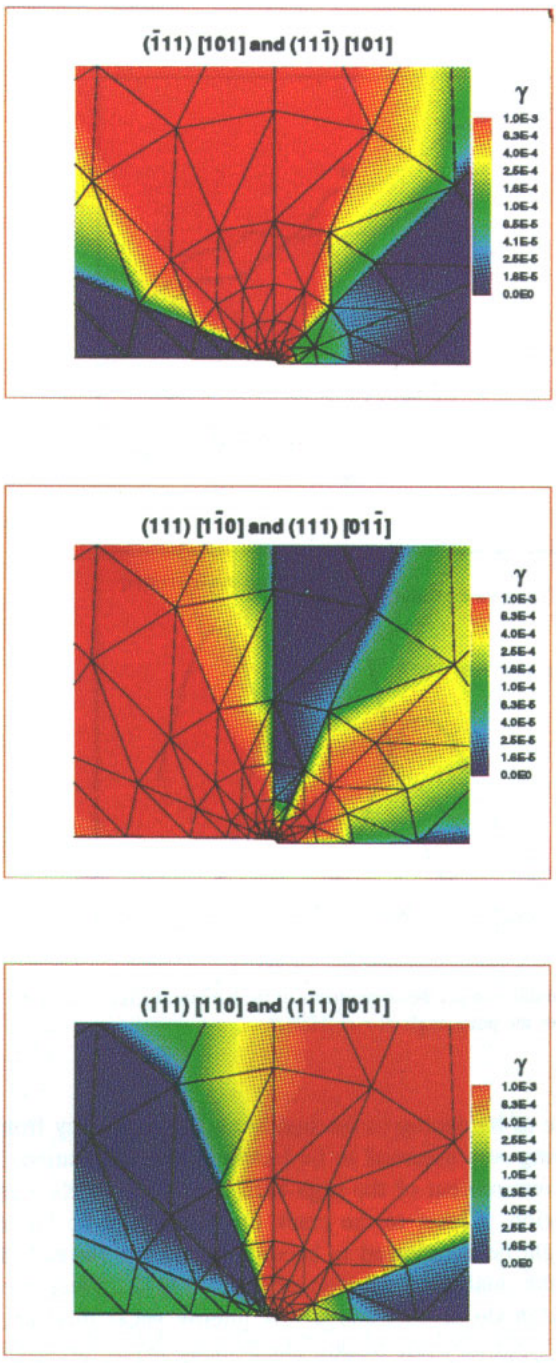

Figure 19. Isocontours of slip strain in the vicinity of the crack tip.

The results of Mohan and co-workers (1992a,b) provide a noteworthy counterpoint to the above picture. Because of the hardening law adopted in their computations, the

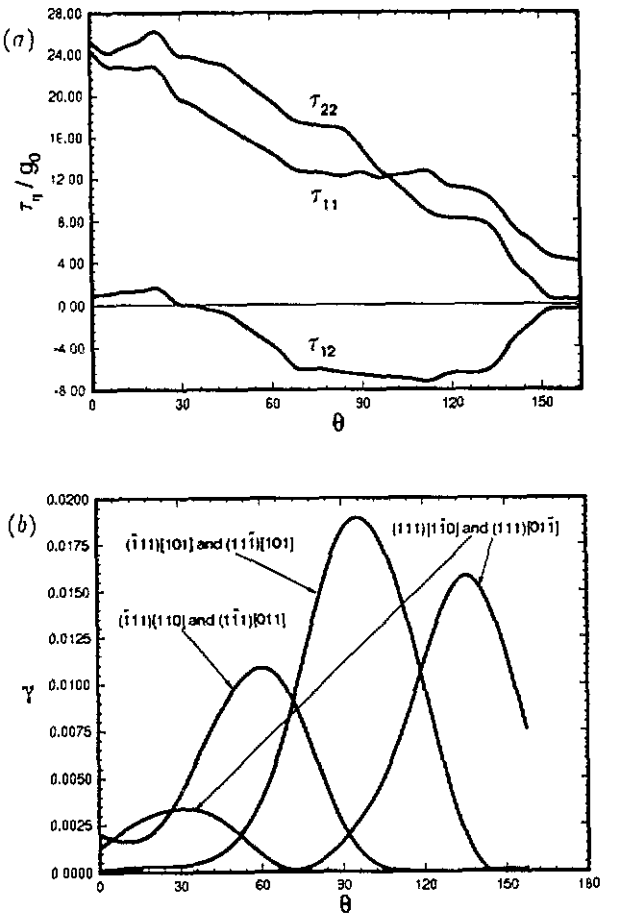

Figure 20. Variation of (*a*) the components of the Kirchhoff stress tensor and (*b*) the slip strains as a function of the polar angle at $r = 0.001R$.

crystal exhibits a rapid rate of hardening in the small-strain region away from the crack tip. Since, in addition, hardening was assumed to be isotropic, the calculations of Mohan and co-workers (1992a,b) are reminiscent of the high-hardening limit of Rice and Saaedvafa's (1988) solution in that region. Closer to the crack tip, the crystal no longer hardens and Rice's (1987) solution might be anticipated to become dominant. Instead, the calculations differ substantially from the analytical solution of Rice (1987). Thus, the system (211) $[1\bar{1}\bar{1}]$ gives rise to a kink mode at 40°, and a less intense shear mode at 130°. A less intense kink mode at 112° and an even weaker shear mode at 22° are contributed by the (011) $[1\bar{1}1]$ system. Finally, slip on the $(2\bar{1}\bar{1})$ [111] system gives rise to a shear mode at about 70° to the plane of the crack. Finite lattice rotations, which are neglected in Rice's analysis, may account for these discrepancies. Indeed, the calculations reveal the presence of substantial lattice rotations which tend to concentrate in the direction of the kink modes. The axis of lattice rotation is nearly uniform throughout the crystal and parallel to the crack front. Finite rotations of the lattice may induce geometrical hardening or softening

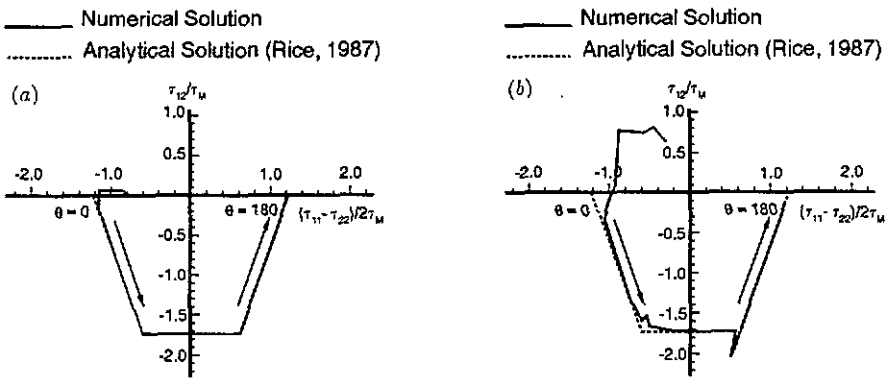

Figure 21. Trajectory of the Kirchhoff stress at: (*a*) $r = 0.18R$; (*b*) $r = 0.001R$.

(Asaro 1983), depending on the direction of rotation. Localization instabilities induced by geometrical softening may in turn have a marked influence on the prevailing deformation pattern (Asaro and Rice 1977). These effects cannot be properly accounted for unless finite deformations and, specifically, finite lattice rotations are rigorously included in the formulation. Interestingly, the calculations of Mohan and co-workers (1992a,b) are in good agreement with the experimental observations of Shield and Kim (1990) on Fe–Si crystals, which attests to the adequacy of the modeling for this class of materials.

Acknowledgments

The support of the US Office of Naval Research through grant N00014-90-J-1758 is gratefully acknowledged. MO is grateful for support received while on visit at the LPMTM of the Université Paris Nord, where some aspects of the work reported in this paper were partly completed. MO is also indebted to P Franciosi for many helpful discussions.

References

Ambrosi P, Göttler E and Schwink Ch 1974 On dislocation arrangement and flow stress of [111] copper single crystals deformed in tension *Scr. Metall.* **8** 1093

Asaro R J 1983 Micromechanics of crystals and polycrystals *Adv. Appl. Mech.* **23** 1

Asaro R J and Rice J R 1977 Strain localization in ductile single crystals *J. Mech. Phys. Solids* **25** 309

Baird J D and Gale B 1965 Attractive dislocation intersections and work hardening in metals *Phil. Trans. R. Soc.* A **257** 553

Bassani J L 1990 Single crystal hardening *Appl. Mech. Rev.* **45** 320

Bassani J L and Wu T Y 1989 Latent hardening in single crystals: part 2. Analytical characterization and predictions (University of Pennsylvania)

Cahn R W 1951 Slip and polygonization in aluminum *J. Inst. Met.* **79** 129

Chang Y W and Asaro R J 1981 An experimental study of shear localization in aluminum–copper single crystals *Acta Metall.* **29** 241

Ciarlet P G 1978 *The Finite Element Method for Elliptic Problems* (Amsterdam: North-Holland)

Crane H L Jr, Gibbs N E, Poole W G and Stockmeyer P K 1976 Matrix Bandwidth and Profile Reduction, ACM-CALGO Algorithm 508 *ACM Trans. Math. Software* **2** 375

Crisfield M A 1991 *Non-Linear Finite Element Analysis of Solids and Structures* vol. 1 (New York: Wiley)

Devloo P, Oden J T and Strouboulis T 1987 Implementation of an adaptive refinement technique for the SUPG algorithm *Comput. Meth. Appl. Mech. Eng.* **61** 339

Diaz A R, Kikuchi N and Taylor J E 1983 A method of grid optimization for finite element methods *Comput. Meth. Appl. Mech. Eng.* **41** 29

Essmann U and Rapp M 1973 Slip in copper crystals following weak neutron bombardment *Acta Metall.* **21** 1305

Foreman A J E and Makin M J 1966 Dislocation movement through random arrays of obstacles *Phil. Mag.* **14** 911

—— 1967 Dislocation movement through random arrays of obstacles *Can. J. Phys.* **45** 511

Franciosi P 1983 Glide mechanisms in BCC crystals: an investigation of the case of α-iron through multislip and latent hardening tests *Acta Metall.* **31** 1331

—— 1985a The concepts of latent hardening and strain hardening in metallic single crystals *Acta Metall.* **33** 1601

—— 1985b FCC single crystal hardening: anisotropy and stacking fault energy *Proc. ICSMA Symp. (Montreal, Canada 1985)* p 281

—— 1988 On flow and work hardening expression correlations in metallic single crystal plasticity *Revue Phys. Appl.* **23** 383

Franciosi P, Berveiller M and Zaoui A 1980 Latent hardening in copper and aluminium single crystals *Acta Metall.* **28** 273

Franciosi P and Zaoui A 1982 Multislip in F. C. C. crystals: a theoretical approach compared with experimental data *Acta Metall.* **30** 1627

Friedrichs J and Haasen P 1975 Ternary solution-hardening of copper single crystals *Phil. Mag.* **31** 863

Gibbs N E, Poole W .G Jr and Stockmeyer P K 1976 An algorithm for reducing the bandwidth and profile of a sparse matrix *SIAM J. Numer. Anal.* **13** 235

Gillis P P and Gilman J 1965 Dynamical dislocation theory of crystals plasticity. II. Easy glide and strain hardening *J. Appl. Phys.* **36** 3380

Grosskreutz J C and Mughrabi H 1975 Description of the work-hardened structure at low temperature in cyclic deformation *Constitutive Equations in Plasticity* ed A S Argon (Cambridge, MA: MIT Press) p 251

Havner K S 1973 On the mechanics of crystalline solids *J. Mech. Phys. Solids* **21** 383

Hill R and Rice J R 1972 Constitutive analysis of elastic-plastic crystals at arbitrary strain *J. Mech. Phys. Solids* **20** 401

Hughes T J R and Taylor R L 1978 Unconditionally stable algorithm for quasi-static elasto visco-plastic finite element analysis *Comput. Struct.* **8** 169

Johnston W G and Gilman J J 1959 Dislocation velocities, dislocation densities and plastic flow in lithium flouride crystals *J. Appl. Phys.* **30** 129

—— 1960 Dislocation multiplication in lithium flouride crystals *J. Appl. Phys.* **31** 632

Kocks U F 1960 Polyslip in single crystals *Acta Metall.* **8** 345

—— 1964 Latent hardening and secondary slip in aluminum and silver *Trans. Metall. Soc. AIME* **230** 1160

—— 1966 A statistical theory of flow stress and work-hardening *Phil. Mag.* **13** 541

—— 1970 The relation between polycrystal deformation and single-crystal deformation *Metall. Trans.* **1** 1121

Kocks U F and Brown T J 1966 Latent hardening in aluminum *Acta Metall.* **14** 87

Kovács I and Zsoldos L 1973 *Dislocation and plastic deformation* (Oxford: Pergamon)

Kuhlmann-Wilsdorf D 1989 Theory of plastic deformation: properties of low energy dislocation structures *Mater. Sci. Eng.* A **113** 1

Lee E H 1969 Elastic-plastic deformation at finite strains *J. Appl. Mech. Am. Soc. Mech. Eng.* **36** 1

Li J C M 1961 Cross slip and cross climb induced by a locked dislocation *J. Appl. Phys.* **32** 593

Mandel J 1972 *Plasticité classique et viscoplasticité (Lecture Notes, International Centre for Mechanical Science Udine)* (Berlin: Springer)

Marsden J E and Hughes T J R 1983 *Mathematical Foundations of Elasticity* (Englewood Cliffs, NJ: Prentice-Hall)

Miura S, Kuriyama Y and Yoshitaka S 1977 Deformation behavior of (100) oriented copper single crystals *Trans. Japan. Inst. Metals* **18** 852

Mohan R, Ortiz M and Shih C F 1992a An analysis of cracks in ductile single crystals: part I—Antiplane shear *J. Mech. Phys. Solids* **40** 291

—— 1992b An analysis of cracks in ductile single crystals: part II—Mode-I loading *J. Mech. Phys. Solids* **40** 315

Moran B, Ortiz M and Shih C F 1990 Formulation of implicit finite element methods for multiplicative finite deformation plasticity *Int. J. Num. Meth. Eng.* **29** 483

Mughrabi H 1975 Description of the dislocation structure after unidirectional deformation at low temperatures *Constitutive Equations in Plasticity* ed A S Argon (Cambridge, MA: MIT Press) p 199

Needleman A, Asaro R J and Lemonds J 1985 Finite element analysis of crystalline solids *Comput. Meth. Appl. Mech. Eng.* **52** 689

Oden J T, Demkowicz L, Strouboulis T and Devloo P 1986 Adaptive methods for problems in solid and fluid mechanics *Accuracy Estimates and Adaptive Refinements in Finite Element Computations* ed I Babuska, O C Zienkiewicz, J Gago and E R de A Oliveira (New York: John Wiley)

Ortiz M and Popov E P 1982 A statistical theory of polycrystalline plasticity *Proc. R. Soc.* A **379** 439

Ortiz M and Quigley J J IV 1991 Adaptive mesh refinement in strain localization problems *Comput. Meth. Appl. Mech. Eng.* **90** 781

Pierce D, Asaro R J and Needleman A 1983 Material rate dependence and localized deformation in crystalline solids *Acta Metall.* **31** 1951

Ramaswami B, Kocks U F and Chalmers B 1965 Latent hardening in silver and Ag–Au alloy *Trans. Metall. Soc. AIME* **233** 927

Résibois P and de Leener M 1977 *Classical Kinetic Theory of Fluids* (New York: Wiley)

Rice J R 1970 On the structure of stress-strain relations for time-dependent plastic deformation in metals *J. Appl. Mech. Am. Soc. Mech. Eng.* **37** 728

—— 1971 Inelastic constitutive relations for solids: an internal-variable theory and its application to metal plasticity *J. Mech. Phys. Solids* **19** 433

—— 1987 Tensile crack tip fields in elastic-ideally plastic crystals *Mech. Mater.* **6** 317

Rice J R and Nikolic R 1985 Anti-plane shear cracks in ideally plastic crystals *J. Mech. Phys. Solids* **33** 595

Rice J R and Saeedvafa M 1988 Crack tip singular fields in ductile single crystals with Taylor power-law hardening. I: Anti-plane shear *J. Mech. Phys. Solids* **36** 189

Sackett J S, Kelly J M and Gillis P P 1976 A probabilistic approach to polycrystalline plasticity *Proc. 2nd Int. Conf. on Mechanical Behaviour of Materials* (Boston, USA) vol 1 p 28

Saeedvafa M and Rice J R 1989 Crack tip singular fields in ductile single crystals with Taylor power-law hardening. II: Plane strain *J. Mech. Phys. Solids* **37** 673

Schwink C and Göttler E 1976 Dislocation interactions, flow stress and initial work hardening of copper single crystals with [100] axis orientation *Acta Metall.* **24** 173

Shield T W and Kim K-S 1990 private communication

Simó, J and Pister K S 1984 Remarks on rate constitutive equations for finite deformation problems: computational implications *Comput. Meth. Appl. Mech. Eng.* **46** 201

Simó J C and Taylor R L 1985 Consistent tangent operators for rate independent elasto-plasticity *Comput. Meth. Appl. Mech. Eng.* **48** 101

Sloan S W 1987 A fast algorithm for constructing Delaunay triangulations in the plane *Adv. Eng. Software* **9** 34

Teodosiu C 1970 *Proc. Conf. on Fundamental Aspects of Dislocation Theory (Washington 1969)* ed J A Simmons *et al* National Bureau of Standards Special Publication **2** 837

—— 1982 *Elastic Models of Crystal Defects* (Berlin: Springer)

Teodosiu C and Sidoroff F 1976 A finite theory of the elastoviscoplasticity of single crystals *Int. J. Eng. Sci.* **14** 713

Wu T-Y, Bassani J L and Laird C 1989 Latent hardening in single crystals: part 1. Experimental characterization (University of Pennsylvania)